AGU PUBLICATIONS

Geochemistry, Geophysics, Geosystems

RESEARCH ARTICLE
10.1002/2014GC005517

Magmatic plumbing at Lucky Strike volcano based on olivine-hosted melt inclusion compositions

V. D. Wanless[1], A. M. Shaw[2], M. D. Behn[3], S. A. Soule[3], J. Escartín[4], and C. Hamelin[5]

[1]Department of Geosciences, Boise State University, Boise, Idaho, USA, [2]Lorax Environmental Services Ltd., Vancouver, British Columbia, Canada, [3]Department of Geology and Geophysics, Woods Hole Oceanographic Institution, Woods Hole, Massachusetts, USA, [4]Equipe de Géosciences Marines, IPGP, CNRS-IPGP, Paris, France, [5]Centre for Geobiology, University of Bergen, Bergen, Norway

Key Points:
- Vapor saturation pressures show crystallization occurs from mantle to seafloor
- Trace element ratios suggest that melts are not homogenized prior to entrapment
- Models suggest melts can be explained by variations in source/extent of melting

Supporting Information:
- Supporting Information figures

Correspondence to:
V. D. Wanless,
dwanless@whoi.edu

Citation:
Wanless, V. D., A. M. Shaw, M. D. Behn, S. A. Soule, J. Escartín, and C. Hamelin (2015), Magmatic plumbing at Lucky Strike volcano based on olivine-hosted melt inclusion compositions, *Geochem. Geophys. Geosyst.*, *16*, 126–147, doi:10.1002/2014GC005517.

Received 23 JUL 2014
Accepted 15 DEC 2014
Accepted article online 19 DEC 2014
Published online 20 JAN 2015

Abstract Here we present volatile, major, and trace element concentrations of 64 olivine-hosted melt inclusions from the Lucky Strike segment on the mid-Atlantic ridge. Lucky Strike is one of two locations where a crustal melt lens has been seismically imaged on a slow-spreading ridge. Vapor-saturation pressures, calculated from CO_2 and H_2O contents of Lucky Strike melt inclusions, range from approximately 300–3000 bars, corresponding to depths of 0.5–9.9 km below the seafloor. Approximately 50% of the melt inclusions record crystallization depths of 3–4 km, corresponding to the seismically imaged melt lens depth, while an additional ~35% crystallize at depths > 4 km. This indicates that while crystallization is focused within the melt lens, significant crystallization also occurs in the lower crust and/or upper mantle. The melt inclusions span a range of major and trace element concentrations from normal to enriched basalts. Trace element ratios at all depths are heterogeneous, suggesting that melts are not efficiently homogenized in the mantle or crust, despite the presence of a melt lens. This is consistent with the transient nature of magma chambers proposed for slower-spreading ridges. To investigate the petrogenesis of the melt inclusion compositions, we compare the measured trace element compositions to theoretical melting calculations that consider variations in the melting geometry and heterogeneities in the mantle source. The full range of compositions can be produced by slight variations in the proportion of an Azores plume and depleted upper mantle components and changes in the total extent of melting.

1. Introduction

Mid-ocean ridge (MOR) magmas can be influenced by a variety of crustal and upper mantle processes, which alter magma compositions prior to eruption on the seafloor. These processes include chemical exchange during melt extraction from the mantle [*Kelemen et al.*, 1995, 1997; *Stracke and Bourdon*, 2009; *Katz and Weatherley*, 2012]; melt rock reaction during ascent through the crust [*Kelemen et al.*, 1995, 1997; *Lissenberg and Dick*, 2008; *Stracke and Bourdon*, 2009; *Katz and Weatherley*, 2012]; and fractional crystallization [*Sinton and Detrick*, 1992; *Perfit et al.*, 1994; *Perfit and Chadwick*, 1998]. When present, a shallow crustal melt lens may provide a region where significant fractional crystallization and melt homogenization can occur [e.g., *Rubin and Sinton*, 2007]. However, homogenization is not restricted to the shallow crust [e.g., *Wanless and Shaw*, 2012] and pooling of melts at any depth may obscure primary geochemical signatures, making it difficult to determine the composition and petrogenesis of magmas in the lower crust and mantle. One method to determine the petrologic evolution of magmas prior to homogenization is to analyze melt inclusions, droplets of melt that are entrapped in crystallizing phenocrysts. For most elements, olivine-hosted melt inclusions are effectively isolated from the host magma and thus have the potential to retain melt compositions from the early stages of magmatic evolution, prior to melt homogenization.

The presence of a nearly continuous, shallow melt lens at fast-spreading and intermediate-spreading rate ridges is thought to reflect a robust and quasi steady state magma supply from the mantle [*Morgan and Chen*, 1993]. Persistent melt lenses are believed to be the primary region of melt pooling, homogenization, and differentiation in the crust at MORs [e.g., *Sinton and Detrick*, 1992]. Extensive geochemical evidence suggests that the melt lens is a region where melts undergo mixing, crystallization, and repeated replenishment by relatively primitive mantle melts, thus buffering and efficiently homogenizing the compositions of lavas erupted on the seafloor [*Sinton and Detrick*, 1992; *Perfit and Chadwick*, 1998; *Rubin and Sinton*, 2007; *Rubin*

et al., 2009; *O'Neill and Jenner*, 2012]. Geophysical studies suggest that most eruptions on fast-spreading ridges are sourced from the melt lens, which is further supported by volatile concentrations of erupted lavas that have maximum saturation pressures consistent with the top of the melt lens [*Le Roux et al*., 2006; *Soule et al*., 2012]. Thus, at fast-spreading to intermediate-spreading ridges, processes occurring within the shallow melt lens (including melt differentiation and homogenization) have a large influence on the compositions of melts erupting at the surface.

At slower-spreading rates, geophysical studies indicate that a shallow steady state melt lens is often absent [*Detrick et al*., 1990; *Calvert*, 1997] and geochemical evidence for melt pooling is less clear. Studies of lavas [*Rubin and Sinton*, 2007] and melt inclusions [*Sobolev and Shimizu*, 1993; *Shimizu*, 1998; *Laubier et al*., 2012] from the slow-spreading Mid-Atlantic Ridge (MAR) display a wide range of compositions, suggesting that there is no centralized region of melt homogenization in the crust or upper mantle. This is consistent with the general absence of a melt lens along most of the MAR. However, there are two locations on a slow-spreading ridge where a shallow melt lens has been imaged seismically; the Lucky Strike segment of the MAR, located south of the Azores hotspot, [*Singh et al*., 2006] and the Reykjanes Ridge near the Iceland Hotspot [e.g., *Navin et al*., 1998]. Thus, an outstanding question at slow-spreading ridges is how variable are melt compositions at robust magmatic segments of the MAR where a magma lens is present.

Some insight into this question can be gained by examining ultraslow spreading ridges. There is no seismic evidence for a melt lens at ultraslow-spreading ridges; though few such studies have been attempted due to the difficulty in conducting seismic studies in the greater water depths and rough terrain characteristic of these settings. A wide range of compositions are observed in lavas erupted on the ultraslow-spreading Southwest Indian Ridge, suggesting inefficient melt homogenization [*Standish et al*., 2008] similar to slow-spreading systems. By contrast, recent studies found remarkably homogeneous trace element ratios in melt inclusions from several individual magmatic centers on the ultraslow-spreading Gakkel Ridge [*Shaw et al*., 2010; *Wanless et al*., 2014], suggesting melt homogenization has occurred. Combining trace element data with depth constraints from vapor saturation pressures derived from H_2O–CO_2 systematics [*Dixon et al*., 1995], these melt inclusion studies concluded that at many large volcanic centers, melt pooling and homogenization must have occurred in the mantle prior to the melts ascending through the oceanic crust. However, melt inclusions and lava compositions erupted at individual volcanic centers can be variable with respect to adjacent volcanic centers [*Wanless et al*., 2014], which is consistent with Southwest Indian Ridge studies.

Here, we combine volatile contents with major and trace element concentrations of 64 naturally glassy, olivine-hosted melt inclusions from the Lucky Strike segment to examine (1) the distribution of crystallization on a slow-spreading ridge segment with a shallow melt lens; (2) the compositional evolution of melts as they ascend through the crust; and (3) melt heterogeneity beneath Lucky Strike volcano. Our data are compared to similar geochemical suites of melt inclusion compositions from fast-spreading, intermediate-spreading, and ultraslow-spreading ridges in order to evaluate melt pooling and crystallization in the crust and upper mantle across mid-ocean ridges with a range of spreading rates.

2. Previous Studies at Lucky Strike

The Lucky Strike segment is located south of the Azores hotspot on the MAR (Figure 1). The segment is ~70 km in length, has a mean depth of 2580 m, and is bound by nontransform offsets [*Parson et al*., 2000]. At the middle of the Lucky Strike segment, a central volcano rises to ~1660 m water depth [*Cannat et al*., 1999; *Escartín et al*., 2001]. The central volcano contains a central depression, infilled by lava, surrounded by three highs that correspond to rifted volcanic cones [*Fouquet et al*., 1998; *Humphris et al*., 2002; *Escartín et al*., 2014] (Figure 1). One of the largest active basalt hosted, deep-sea hydrothermal vent fields is located at the summit of this central volcano [*Langmuir et al*., 1997; *Ondréas et al*., 2009; *Barreyre et al*., 2012].

Numerous geophysical studies have been carried out on the Lucky Strike segment. At the segment scale, there is a "bull's-eye" mantle Bouguer gravity low, suggesting focused upwelling and melt delivery from the mantle to the center of the ridge segment [*Detrick et al*., 1995; *Thibaud et al*., 1998; *Cannat et al*., 1999; *Escartín et al*., 2001]. Crustal thickness varies from 7–7.5 km at the segment center to 5–6 km at segment ends [*Seher et al*., 2010], consistent with focused melt delivery to the segment center. Microseismicity indicates that the lithosphere thickens from ~6.5 km at the segment center to ~10 km at the segment end [*Dusunur et al*., 2009].

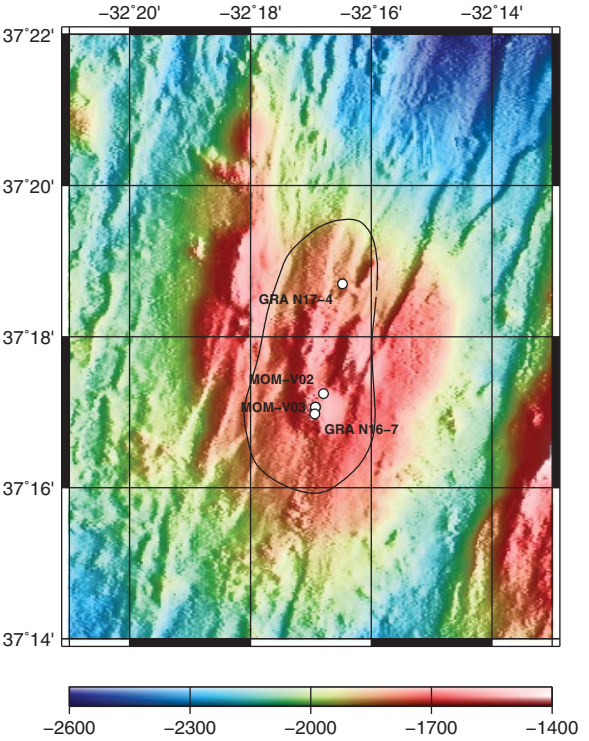

Figure 1. Bathymetric map of the Lucky Strike region. White circles indicate sample locations. Black line shows approximate outline of the seismically imaged melt lens [*Singh et al*., 2006].

Seismic reflection surveys at the segment center image a melt lens in the mid-crust beneath Lucky Strike [*Singh et al*., 2006]. Recent microseismicity data also suggest that fluid flow associated with the hydrothermal field likely roots at the roof of the AMC [*Crawford et al*., 2013]. In contrast to the narrow, shallow melt lenses observed at fast-spreading centers, the Lucky Strike melt lens is deeper (∼3.4 km below seafloor (bsf)) and wider (∼3 km across) and, although the seismic experiment did not span the full length of the segment, the melt lens appears to be confined to the central region of the segment. The melt lens is overlain by a central volcano [*Singh et al*., 2006] (Figure 1), supporting the notion of enhanced melt supply to the segment center. There is a low-velocity zone in the lower crust below the melt lens, which can be interpreted to reflect either elevated crustal temperatures (∼800 to 1000°C) or <1% remnant melt in the lower crust [*Seher et al*., 2010]. Above the melt lens (from 2 to 3.5 km bsf), there is a low-velocity zone, attributed to high porosity associated with normal faulting and/or the presence of fresh porous lava on-axis [*Seher et al*., 2010; *Arnulf et al*., 2014]. There is also a region of thicker crust offset to the west of the central volcano, suggesting a past period of enhanced magmatism to the segment center [*Seher et al*., 2010].

Gale et al. [2011] present major and trace element compositions and radiogenic isotope ratios of basalts erupted along the length of the segment. Mid-ocean ridge basalts (MORBs) with transitional compositions (T-MORB) between normal MORB (N-MORB) and enriched MORB (E-MORB) are erupted along the entire length of the segment, while E-MORB lavas are only observed at the segment center [*Gale et al*., 2011]. No N-MORB lavas are observed anywhere along the segment [*Gale et al*., 2011]. Based on a combination of seafloor observations and lava chemistry, E-MORB lavas underlie T-MORB lavas [*Langmuir et al*., 1997], leading to the hypothesis that the most recent melts are T-MORB in composition [*Gale et al*., 2011]. Homogeneous He and Ne isotope ratios in basalts from the length of the ridge axis indicate significant melt homogenization prior to eruption, favoring a model in which melts are focused beneath the center of the Lucky Strike segment of the MAR and then redistributed along-axis by dike propagation [*Moreira et al*., 2011]. In contrast, Hf, Pb, Sr, and Nd isotope ratios are variable, suggesting inefficient melt homogenization [*Hamelin et al*., 2013] and/or differences in the relative diffusivities of these elements in silicate melts.

3. Samples, Methods, and Data Corrections

3.1. Samples

Sixty-four naturally glassy, olivine-hosted melt inclusions from four basaltic samples erupted at the central volcano on the Lucky Strike segment of the MAR were analyzed for volatile and major element concentrations. Fifteen of these melt inclusions were measured for trace element concentrations using ion microprobe techniques. The basaltic host rocks were not available for this study; however, major element compositions indicate that the lavas are E-MORB. Sample locations and depths are provided in Table 1 and shown in Figure 1. All four basalt samples were collected near the summit of the central volcano, above the seismically imaged melt lens during two cruises on the N/O Atalante (GRAVILUCK, 2006; Bathyluck, 2008). Two of the lavas were erupted at the southernmost mound of Lucky Strike (MOM-V02; MOM-V03), one was collected just south of the summit cones (GRA N16-7), and one was collected north of the summit cones

Table 1. Sample Locations

Sample Name	Latitude	Longitude	Seafloor Depth (m)	Geologic Feature
GRA N16-7	37.2829 N	32.2822 W	1551	South of Cone
GRA N17-4	37.3116 N	32.2745 W	1779	North of Lava Lake
MOM-V02	37.2874 N	32.2798 W	1741	Southern Cone
MOM-V03	37.2844 N	32.2820 W	1557	Top of Southern Cone

(GRA N17-4) (Figure 1). The lavas were crushed and olivines were handpicked, mounted in epoxy, and polished individually to expose each melt inclusion. Polished olivines were then mounted in indium for analyses.

3.2. Geochemical Analyses

Melt inclusions were analyzed for volatile contents (CO_2, H_2O, Cl, F, and S; Table 2) using the 1280 ion microprobe at WHOI following methods outlined in *Hauri et al*. [2002] and *Shaw et al*. [2008]. Measurements were made using a 1–2 nA rastered (15–20 μm) Cs^+ beam. Calibration curves were made for each session and the MORB glass standard ALV-519-4-1 was measured routinely throughout the sessions to monitor instrumental drift. Background H_2O concentrations were below detection limits during both volatile sessions based on analyses of an internal synthetic forsterite standard.

Melt inclusions (Table 3) and host-olivines (supporting information Table S1) were measured for major element concentrations using a JOEL-JXA-8200 electron microprobe at MIT. Melt inclusions were analyzed using a beam intensity of 10 nA, a spot size of 10 μm, and an accelerating voltage of 15 kV. Counting times were 40 s for all elements except Na, which was measured for 5 s to minimize Na loss. Host-olivine compositions were measured using a spot size of 1 μm. Three analyses were collected on each olivine, along transects from the edge of the melt inclusion to the grain boundary to test for compositional zoning. No zoning was observed and thus the three analyses from each olivine grain were averaged. Major element compositions of olivines are provided in supporting information Table S1. Trace element concentrations of fifteen melt inclusions were measured using a 6f ion microprobe at Arizona State University. Methods of both techniques are discussed in *Wanless et al*. [2014] and results are provided in Table 4.

3.3. Data Corrections

All melt inclusion data were corrected for post entrapment olivine crystallization and, if present, shrinkage bubbles (supporting information Table S2). To correct for post entrapment crystallization, olivine was iteratively added back into the melt composition using a Fe-Mg K_D of 0.3 and a Fe^{3+}/total FeO of 0.15 [*Kelley and Cottrell*, 2009] until the melt was in equilibrium with the host-olivine phenocrysts [*Danyushevsky*, 2002]. In general, the amount of olivine added back into the melt composition was $<$15% (supporting information Table S2). Melt inclusion compositions were also corrected for the presence of shrinkage bubbles, which can form due to the differential melt contraction of the inclusion and the host crystal [*Roedder*, 1984]. The calculated vapor content (CO_2 and H_2O) was then added back to the glass composition following the method of *Shaw et al*., [2008]. Melt inclusion and vapor bubble dimensions are provided in supporting information Table S2, along with precorrected volatile and major element data.

4. Geochemical Results

CO_2 and H_2O contents (Table 2) range from 153 to 1498 ppm and 0.30 to 0.51 wt %, respectively (Figure 2). Based on experimental results, *Dixon et al*. [1995] showed that CO_2 and H_2O contents in a melt can be used to determine minimum pressures of equilibration. Because magmas from which the melt inclusions are derived are likely vapor-saturated [*Wanless and Shaw*, 2012], the equilibration pressures can be used to infer the pressure of crystallization beneath a MOR axis. Following this approach, we calculated equilibration pressures for the Lucky Strike melt inclusions and converted them to the depth of crystallization below the seafloor (Table 2). Calculations included the pressure of the overlying water column based on the depth of eruption, and assumed a constant crustal density of 2.8 g cm^{-3} (average density of oceanic crust at Lucky Strike based on seismic profiles from *Seher et al*., 2010]. Different estimates for water depth and/or crustal density result in limited shifts in the pressure estimate, but maintain the relative pressure differences.

There is a wide range of crystallization pressures (327–2931 bars) in the four Lucky Strike samples (Figure 2), with corresponding crystallization depths of ~600–9900 m (bsf). To quantify the distribution of

Table 2. Volatile Contents

Sample Name	H2O (wt%)	CO2 (ppm)	F (ppm)	S (ppm)	Cl (ppm)	Pressure (bars)	Depth (m)
GRA N16-7_3	0.34	1219	297	732	60	2201	7065
GRA N16-7_4	0.36	1145	288	784	26	2117	6774
GRA N16-7_5	0.37	488	269	822	13	937	2705
GRA N16-7_6	0.37	289	381	454	36	576	1460
GRA N16-7_8	0.33	999	309	810	35	1822	5757
GRA N16-7_10	0.39	839	389	734	413	1605	5008
GRA N16-7_12	0.36	906	403	642	37	1681	5272
GRA N16-7_13a	0.35	606	173	715	74	1138	3400
GRA N16-7_13b	0.35	949	156	722	59	1751	5513
GRA N16-7_14	0.37	153	118	347	18	327	603
GRA N16-7_15	0.35	453	400	646	23	862	2448
GRA N16-7_17	0.34	663	217	730	57	1210	3646
GRA N16-7_18	0.35	684	220	768	64	1263	3829
GRA N17-4_19	0.32	702	317	942	68	1266	3762
GRA N17-4_20	0.33	500	364	821	87	937	2629
GRA N17-4_21	0.32	505	294	1005	88	937	2628
GRA N17-4_24	0.34	914	318	940	109	1673	5166
GRA N17-4_25	0.32	1229	554	771	38	2142	6783
GRA N17-4_27a	0.34	462	352	812	86	883	2443
GRA N17-4_27b	0.33	504	348	827	80	949	2669
GRA N17-4_28a	0.34	521	293	833	91	1007	2869
GRA N17-4_28b	0.34	478	316	824	89	906	2521
GRA N17-4_29	0.35	445	288	851	89	863	2373
GRA N17-4_30	0.30	668	331	743	141	1235	3657
GRA N17-4_33a	0.35	323	202	602	52	631	1573
GRA N17-4_33b	0.32	438	197	705	71	803	2167
GRA N17-4_34	0.31	830	294	721	125	1473	4476
GRA N17-4_35a	0.35	494	245	817	85	961	2710
GRA N17-4_35b	0.32	637	182	798	55	1207	3559
GRA N17-4_36	0.34	639	336	1005	103	1181	3471
GRA N17-4_4	0.37	337	269	671	80	729	1910
GRA N17-4_5	0.36	320	331	654	74	693	1786
GRA N17-4_6	0.37	352	315	651	78	761	2023
GRA N17-4_7	0.34	289	249	588	62	628	1564
GRA N17-4_7b	0.35	316	252	583	62	684	1755
GRA N17-4_9	0.36	342	238	652	78	739	1945
GRA N17-4_10	0.34	293	396	698	74	637	1593
GRA N17-4_12	0.38	303	313	624	98	660	1673
GRA N17-4_13	0.35	513	330	911	106	1089	3154
MOM-V02_1	0.44	438	98	554	87	942	2660
MOM-V02_2	0.50	538	51	765	68	1150	3375
MOM-V02_3	0.46	907	270	512	74	1867	5847
MOM-V02_4	0.49	541	220	652	94	1156	3397
MOM-V02_5	0.45	567	76	602	77	1204	3563
MOM-V02_8	0.38	1250	191	545	13	2492	8004
MOM-V02_9	0.39	1070	250	495	8	2167	6884
MOM-V02_10	0.40	699	209	574	15	1464	4458
MOM-V02_11	0.43	565	76	597	49	1200	3547
MOM-V02_12	0.43	484	137	635	16	1035	2979
MOM-V02_13	0.43	943	184	571	16	1934	6079
MOM-V02_13b	0.40	915	246	556	16	1878	5885
MOM-V02_15	0.41	575	180	590	−2	1217	3606
MOM-V02_16	0.46	479	39	697	62	1027	2951
MOM-V02_17	0.49	530	134	778	56	1134	3322
MOM-V02_18	0.48	607	125	545	247	1288	3851
MOM-V02_21	0.51	538	52	815	80	1152	3384
MOM-V03_22	0.33	323	271	765	56	698	1879
MOM-V03_24	0.41	556	370	600	62	1179	3537
MOM-V03_27	0.45	1498	333	640	20	2931	9580
MOM-V03_28	0.42	952	228	636	14	1949	6192
MOM-V03_35	0.39	742	265	795	111	1547	4806
MOM-V03_40	0.37	1001	392	653	124	2037	6498
MOM-V03_42	0.43	577	106	656	16	1223	3691

crystallization beneath Lucky Strike volcano, we plotted histograms of the melt inclusion crystallization depths binned in 1.5 km intervals for all the Lucky Strike inclusions (Figure 3a) and for each sample individually (Figures 3b–3e). The bin width (W) is chosen based on the statistically optimized bin size for each data

Table 3. Major Element Concentrations

	SiO2	TiO2	Al2O3	FeOt	MnO	MgO	CaO	Na2O	K2O	P2O5	K2O/TiO2	Mg#	Mg#	Temperature[a]	Pressure[a]
Sample Name	wt %	wt %	wt %	wt %	wt %	wt %	wt %	wt %	wt %	wt %		Olivine	Glass	°C	Gpa
GRA N16-7_3	51.08	0.62	14.97	6.63	0.10	10.55	14.17	1.32	0.09	0.07	0.14	0.90	0.74	1230	0.33
GRA N16-7_4	50.86	0.73	14.61	7.08	0.13	10.35	13.90	1.82	0.03	0.06	0.05	0.90	0.72	1251	0.51
GRA N16-7_5	51.02	0.70	14.70	7.14	0.12	10.14	13.90	1.76	0.03	0.05	0.04	0.89	0.72	1251	0.50
GRA N16-7_6	52.70	0.96	14.89	5.79	0.10	10.07	13.09	1.88	0.06	0.03	0.07	0.91	0.76	1189	0.21
GRA N16-7_8	51.13	0.61	14.77	6.52	0.13	10.58	14.32	1.44	0.06	0.06	0.09	0.91	0.74	1226	0.32
GRA N16-7_10	49.31	1.22	15.60	6.60	0.16	9.95	13.80	2.17	0.52	0.22	0.43	0.90	0.73	1238	0.73
GRA N16-7_12	52.53	0.99	14.80	5.88	0.11	10.09	13.03	2.01	0.06	0.08	0.07	0.91	0.75	1193	0.25
GRA N16-7_13a	50.78	0.59	15.20	6.58	0.12	10.67	14.02	1.44	0.10	0.09	0.16	0.91	0.74	1229	0.38
GRA N16-7_13b	50.63	0.59	14.97	6.71	0.13	10.84	14.07	1.48	0.09	0.06	0.15	0.91	0.74	1235	0.41
GRA N16-7_14	51.13	0.61	15.40	6.31	0.11	10.01	14.36	1.57	0.04	0.03	0.07	0.91	0.74	1217	0.33
GRA N16-7_15	52.62	0.97	14.80	5.90	0.10	10.36	12.72	2.02	0.04	0.04	0.04	0.91	0.76	1192	0.24
GRA N16-7_17	50.67	0.61	15.06	6.68	0.10	10.72	14.01	1.44	0.08	0.24	0.13	0.90	0.74	1234	0.39
GRA N16-7_18	50.28	0.62	14.85	6.66	0.11	10.73	14.56	1.55	0.09	0.15	0.15	0.91	0.74	1236	0.43
GRA N17-4_19	50.81	0.70	14.55	7.07	0.11	10.93	13.60	1.70	0.09	0.07	0.13	0.90	0.73	1250	0.49
GRA N17-4_20	50.76	0.70	14.18	7.14	0.14	10.57	14.05	1.78	0.12	0.16	0.17	0.90	0.73	1255	0.52
GRA N17-4_21	51.01	0.75	14.38	6.52	0.11	11.20	13.63	1.82	0.10	0.11	0.14	0.91	0.75	1226	0.40
GRA N17-4_24	50.75	0.76	14.48	7.68	0.13	10.28	13.47	1.81	0.15	0.08	0.20	0.89	0.70	1276	0.65
GRA N17-4_25	51.40	0.95	14.80	6.46	0.08	10.59	13.26	1.99	0.03	0.05	0.04	0.91	0.75	1222	0.40
GRA N17-4_27a	50.83	0.76	14.80	6.88	0.10	10.16	14.30	1.58	0.09	0.09	0.12	0.90	0.72	1243	0.44
GRA N17-4_27b	50.88	0.75	14.70	6.94	0.12	10.20	14.11	1.71	0.10	0.09	0.13	0.90	0.72	1245	0.47
GRA N17-4_28a	50.82	0.77	15.05	6.71	0.12	10.13	14.24	1.56	0.11	0.09	0.15	0.90	0.73	1235	0.42
GRA N17-4_28b	50.68	0.75	14.58	7.05	0.12	10.62	13.90	1.69	0.11	0.10	0.15	0.90	0.73	1250	0.50
GRA N17-4_29	50.75	0.70	15.06	6.62	0.11	10.22	14.08	1.79	0.13	0.12	0.18	0.90	0.73	1232	0.45
GRA N17-4_30	50.58	0.67	15.04	6.21	0.09	10.83	14.25	1.56	0.21	0.20	0.31	0.91	0.76	1216	0.36
GRA N17-4_33a	49.65	0.79	15.97	6.40	0.11	10.94	13.93	1.64	0.07	0.10	0.09	0.91	0.75	1226	0.49
GRA N17-4_33b	49.97	0.75	15.67	6.57	0.11	11.24	13.35	1.74	0.08	0.16	0.11	0.91	0.75	1232	0.51
GRA N17-4_34	50.98	0.83	14.64	6.42	0.08	11.14	13.63	1.66	0.16	0.09	0.20	0.91	0.76	1222	0.37
GRA N17-4_35a	50.68	0.75	14.77	6.88	0.13	10.71	13.78	1.65	0.13	0.11	0.17	0.90	0.74	1243	0.48
GRA N17-4_35b	51.45	0.72	16.15	6.23	0.09	9.59	13.13	2.11	0.10	0.04	0.13	0.90	0.73	1212	0.42
GRA N17-4_36	50.78	0.71	14.19	8.08	0.13	10.65	13.06	1.78	0.12	0.09	0.17	0.89	0.70	1290	0.70
GRA N17-4_4	51.04	0.74	15.45	6.60	0.09	10.10	13.62	1.82	0.11	0.01	0.15	0.90	0.73	1228	0.45
GRA N17-4_5	50.99	0.74	15.05	6.97	0.12	10.33	13.55	1.72	0.10	0.00	0.13	0.90	0.73	1244	0.49
GRA N17-4_6	50.97	0.77	15.16	6.93	0.11	10.04	13.76	1.71	0.12	0.00	0.15	0.90	0.72	1243	0.49
GRA N17-4_7	51.05	0.84	15.72	6.48	0.08	10.52	13.00	1.80	0.08	0.02	0.10	0.91	0.74	1222	0.43
GRA N17-4_7b	50.79	0.90	16.20	6.27	0.09	10.09	13.08	2.09	0.09	0.00	0.10	0.91	0.74	1215	0.48
GRA N17-4_9	51.00	0.70	15.42	6.73	0.11	10.09	13.56	1.88	0.11	0.00	0.16	0.90	0.73	1234	0.48
GRA N17-4_10	50.35	0.75	15.13	6.55	0.10	10.61	14.04	1.97	0.10	0.00	0.13	0.91	0.74	1231	0.50
GRA N17-4_12	49.86	0.78	15.52	7.04	0.12	10.82	13.54	1.79	0.09	0.00	0.12	0.90	0.73	1252	0.62
GRA N17-4_13	50.42	0.81	14.68	7.90	0.12	10.37	13.31	1.83	0.14	0.00	0.17	0.89	0.70	1284	0.72
MOM-V02_1	51.24	0.31	16.00	6.72	0.11	9.87	13.62	1.35	0.15	0.11	0.48	0.90	0.72	1230	0.39
MOM-V02_2	50.35	0.69	14.53	8.29	0.15	9.66	13.55	1.99	0.11	0.10	0.16	0.88	0.68	1299	0.83
MOM-V02_3	51.79	0.92	15.45	6.41	0.09	9.85	12.91	1.81	0.13	0.12	0.14	0.90	0.73	1215	0.37
MOM-V02_4	51.11	0.81	15.02	6.29	0.10	9.79	14.28	1.75	0.19	0.11	0.23	0.90	0.74	1215	0.38
MOM-V02_5	51.11	0.60	15.83	6.37	0.12	9.68	14.12	1.38	0.15	0.12	0.26	0.90	0.73	1218	0.34
MOM-V02_8	50.69	0.64	14.50	7.54	0.15	10.32	13.87	1.71	0.05	0.08	0.07	0.89	0.71	1270	0.59
MOM-V02_9	50.76	0.73	15.34	5.98	0.11	10.53	14.49	1.52	0.03	0.05	0.05	0.91	0.76	1204	0.29
MOM-V02_10	51.05	0.59	15.72	5.79	0.15	9.82	14.74	1.52	0.05	0.10	0.09	0.91	0.75	1196	0.25
MOM-V02_11	50.53	0.60	15.45	6.61	0.12	10.01	14.25	1.73	0.10	0.10	0.17	0.90	0.73	1232	0.46
MOM-V02_12	50.42	0.70	15.28	6.48	0.12	10.44	14.40	1.58	0.05	0.04	0.07	0.91	0.74	1226	0.41
MOM-V02_13	50.89	0.74	15.28	6.18	0.13	9.97	14.46	1.73	0.06	0.06	0.09	0.91	0.74	1212	0.35
MOM-V02_13b	50.75	0.74	14.75	6.34	0.13	10.24	14.78	1.73	0.05	0.04	0.07	0.91	0.74	1220	0.36
MOM-V02_15	50.18	0.67	14.70	7.08	0.15	10.88	14.28	1.53	0.01	0.04	0.02	0.90	0.73	1253	0.51
MOM-V02_16	50.91	0.72	14.51	8.15	0.15	9.27	13.58	2.02	0.11	0.06	0.15	0.87	0.67	1291	0.76
MOM-V02_17	50.75	0.62	14.84	7.97	0.17	9.37	13.48	2.01	0.11	0.10	0.17	0.88	0.68	1284	0.74
MOM-V02_18	50.21	0.68	14.85	7.79	0.13	10.28	13.14	1.92	0.31	0.14	0.45	0.89	0.70	1280	0.78
MOM-V02_21	50.61	0.69	15.09	7.99	0.15	9.52	13.15	2.01	0.12	0.09	0.17	0.88	0.68	1284	0.77
MOM-V03_22	50.78	0.68	14.52	6.69	0.09	11.11	13.87	1.60	0.10	0.17	0.15	0.91	0.75	1235	0.41
MOM-V03_24	50.67	0.78	14.61	6.49	0.12	10.37	14.52	1.76	0.10	0.12	0.12	0.91	0.74	1226	0.41
MOM-V03_27	51.45	1.01	14.66	6.58	0.09	10.28	13.43	1.93	0.04	0.02	0.04	0.90	0.74	1225	0.41
MOM-V03_28	50.42	0.65	14.70	6.80	0.10	11.13	14.20	1.46	0.02	0.05	0.04	0.91	0.74	1239	0.42
MOM-V03_35	50.09	0.83	14.34	7.28	0.11	11.10	13.85	1.72	0.16	0.07	0.19	0.90	0.73	1262	0.61
MOM-V03_40	49.95	0.78	14.67	6.80	0.09	11.03	14.29	1.65	0.16	0.14	0.21	0.91	0.74	1243	0.52
MOM-V03_42	50.70	0.67	15.15	7.01	0.09	9.73	14.37	1.68	0.04	0.08	0.06	0.89	0.71	1248	0.50

[a]Temperature and Pressure calculated using *Lee et al*. [2009].

Table 4. Trace Element Concentrations and Ratios

	B	Sr	Y	Zr	Nb	Ba	La	Ce	Pr	Nd	Sm	Eu	Dy	Yb	La/Yb	Nb/Zr	La/Sm	Ba/La
Sample	ppm	ppm	ppm	ppm	ppm	ppm	ppm	ppm	ppm	ppm	ppm	ppm	ppm	ppm				
GRA N-16-7_3	0.6	80	16	31	3	26	2	5	0.9	4.6	1.5	0.6	2.9	1.7	1.3	0.1	1.4	12.2
GRA N-16-7_4	0.5	75	18	39	2	11	2	6	1.1	5.6	1.9	1.0	3.3	1.8	1.1	0.0	1.0	5.9
GRA N-16-7_10	2.0	273	16	80	24	178	15	27	3.4	14.9	2.4	0.8	3.2	2.2	6.6	0.3	6.2	12.0
GRA N-16-7_13b	0.7	104	16	31	5	34	3	6	0.9	4.4	1.5	0.7	3.2	1.8	1.5	0.2	1.9	12.0
GRA N17-4_1	0.9	231	18	70	24	186	15	28	3.2	13.2	2.9	0.7	3.4	2.0	7.3	0.3	5.0	12.6
GRA N17-4_12	0.6	112	18	43	5	35	4	9	1.4	7.4	2.3	1.0	3.6	1.8	1.9	0.1	1.5	9.9
GRA N17-4_13	0.6	146	21	46	7	46	5	11	1.7	7.6	2.3	1.0	3.9	2.1	2.5	0.1	2.3	8.7
GRA N-17-4_25	0.5	117	19	53	2	15	4	12	1.8	8.7	2.6	1.0	3.5	1.9	2.0	0.0	1.5	3.9
GRA N-17-4_29	0.5	111	16	37	5	36	4	8	1.2	5.3	1.9	0.8	3.1	1.8	2.1	0.1	2.0	9.6
MOM-V02_1	0.5	113	7	20	7	50	3	6	0.8	2.6	0.8	0.5	1.3	0.9	3.3	0.4	4.1	15.8
MOM-V02_1r	0.7	106	7	18	7	46	3	6	0.7	2.7	0.7	0.4	1.3	0.8	3.5	0.4	4.0	15.8
MOM-V02_5	0.4	96	16	31	6	48	3	6	0.9	5.0	1.4	0.5	2.8	1.8	1.8	0.2	2.3	14.6
MOM-V02_13a	0.5	90	19	39	3	18	2	6	1.2	5.4	2.0	0.7	3.4	2.1	1.0	0.1	1.0	8.9
MOM-V02_18	0.7	120	19	36	15	145	5	8	1.0	4.5	1.5	0.6	3.4	2.1	2.5	0.4	3.5	27.0
MOM-V03_22	0.8	101	18	35	6	40	3	7	1.0	5.7	2.4	0.8	3.7	1.9	1.8	0.2	1.4	12.0
MOM-V03_28	0.5	69	17	33	2	12	2	5	0.9	5.0	1.9	0.9	3.2	1.7	1.0	0.1	0.9	7.0
MOM-V03_35	0.6	147	21	54	9	64	6	13	1.6	7.6	2.2	0.7	3.6	2.2	2.7	0.2	2.7	10.8
MOM-V03_40	1.9	126	18	43	10	74	5	8	1.3	6.2	1.9	0.7	3.5	1.9	2.8	0.2	2.7	14.1

set and is derived using the equation $W = 2\ (IQR)*N^{-1/3}$, in which N is the number of samples and IQR is the interquartile range (75th percentile minus 25th percentile) [*Izenman*, 1991]. A bin width of 1.5 km is found to be appropriate for all samples except MOM-V03 (Figure 3e), which requires a 2–2.5 km bin size. For comparison, 1 km and 2.5 km bin intervals are also plotted in supporting information Figure S1.

The major element compositions of the Lucky Strike melt inclusions are variable both between the four different lava samples, and within each individual lava sample (Table 3). Melt inclusion compositions range from 9.27 to 11.24 wt % for MgO; 14.18 to 16.20 wt % for Al_2O_3; 5.79 to 8.29 wt % for FeOt (all iron converted to Fe^{2+}); and 12.72 to 14.78 wt % for CaO (Figure 4). K_2O/TiO_2 ratios, which are used as an indicator of melt heterogeneity [*Langmuir et al.*, 1986; *Sinton et al.*, 1991; *Perfit et al.*, 1994], are variable, ranging from 0.02 to 0.48 (Figure 4). All of the Lucky Strike host-olivines are relatively primitive with Mg numbers (Mg# = Mg/(Mg + Fe) × 100) ranging from 87 to 91 (Table 3). Fractional crystallization trends for each sample calculated from PETROLOG [*Danyushevsky and Plechov*, 2011] are compared to the melt inclusion compositions assuming starting parameters of fO_2 = QFM, temperature = 1250°C, water concentrations from SIMS analyses, and pressures of 1 kbar, consistent with the approximate depth of the melt lens (pressures up to 3 kbar were also calculated, but are not shown). These model calculations indicate that the range of major element concentrations cannot be explained by fractional crystallization from a single parent melt compositions (Figure 4), but rather require up to 10% olivine crystallization from multiple parental melts.

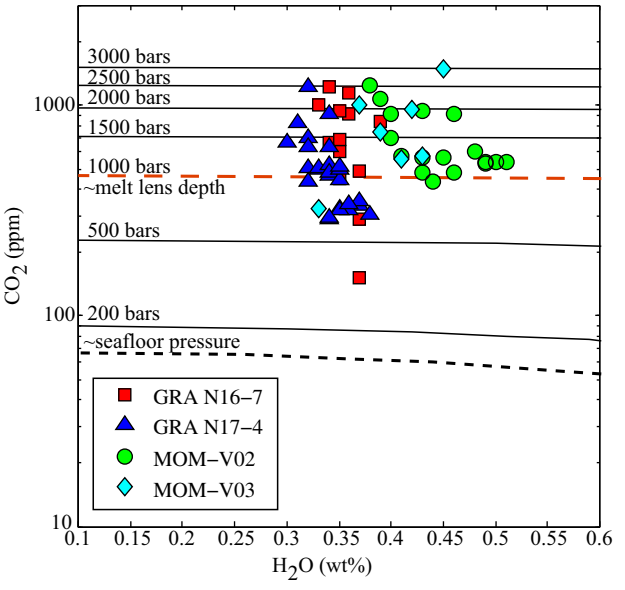

Figure 2. CO_2 (ppm) versus H_2O (wt %) for the Lucky Strike melt inclusions. Vapor saturation curves, calculated using *Newman and Lowenstern* [2002] are shown as solid black lines. The approximate pressure at the seafloor is shown as a black-dashed line and the approximate melt lens pressure is shown as a red-dashed line. Melt inclusions have a wide range of entrapment pressures from 400 to 3000 bars but none have pressures consistent with or less than the pressure at the seafloor.

Trace element concentrations and ratios are also variable in Lucky Strike

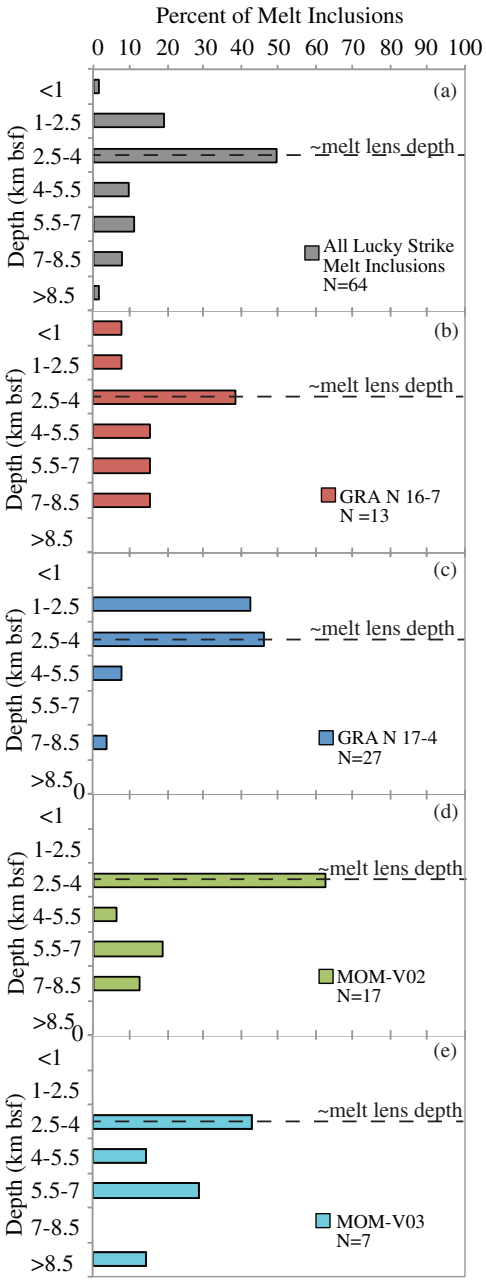

Figure 3. Histograms showing the percentage of melt inclusions entrapped at various depths below the seafloor. The top plot (a) includes all Lucky Strike melt inclusions analyzed in this study (N=64), while the bottom plots (b–e) show the distribution of entrapment pressures from each individual basalt sample. For all samples except MOM-V03, the statistically significant bin size is 1.5 km. MOM-V03 requires a bin size of 2.5 km (see supporting information Figure S1). Greater than 35% of the melt inclusions have crystallization pressures consistent with the depth of the melt lens (3.4 km; *Singh et al.*, 2006] in all four samples. The peak in crystallization is slightly higher in sample GRA N17-4, which may result from crystallization during shallow diking along the ridge axis prior to eruption on the seafloor.

melt inclusions (Table 4). Highly incompatible elements such as Ba and Nb range from 12 to 186 ppm and 1.5 to 24 ppm, respectively. Light rare earth elements (LREE) also have variable compositions, whereas MREE and HREE are less variable with Sm = 0.7–2.9 ppm, and Yb = 0.8–2.2 ppm (Table 4). This is evident in primitive mantle-normalized diagrams (Figure 5), which show that the HREE of the melt inclusions are relatively constant compared to the more incompatible elements.

The Lucky Strike melt inclusions range from N-MORB to E-MORB (Figure 4f). Following nomenclature in *Gale et al.* [2011], we define N-MORB compositions as having $La/Sm_N < 1$ and $K_2O/TiO_2 < 0.11$, while E-MORB have $La/Sm_N > 2$ and $K_2O/TiO_2 > 0.2$. Melt inclusion compositions that fall between these limits are termed transitional MORB (T-MORB). Many of the melt inclusions have trace element patterns that are relatively similar to the average T-MORB lava composition (dashed black line in Figure 5) erupted along the Lucky Strike segment [*Gale et al.*, 2011]. One notable exception is GRA N16-7_10 (Figure 5a), which is characterized by an E-MORB composition that is similar to the average E-MORB lavas reported by *Gale et al.* [2011]. There are also several N-MORB melt inclusions, which is notable because no N-MORB lavas were sampled along the Lucky Strike segment [*Gale et al.*, 2011]. Thus, the melt inclusions sample a wider range of melt compositions than the erupted lavas. Trace element ratios have greater variability than melt inclusions from other MORs [*Wanless and Shaw*, 2012; *Wanless et al.*, 2014], with Ba/La = 4–30; La/Sm = 1.0–6.3; La/Yb = 0.9–6.3; and Nb/Zr = 0.04–0.42, and are more similar to the global variability in basaltic glass data (Figures 6 and 7).

5. Formation of E-, T-, and N-MORB Melts at Lucky Strike

5.1. Previous Studies at Lucky Strike

Many of the Lucky Strike melt inclusions have compositions similar to E- and T-MORB lavas erupted on the Lucky Strike segment [*Gale et al.*, 2011]; however, they extend to N-MORB compositions. A common explanation for the formation of E-MORBs at MORs is melting of a mantle source consisting of an enriched component (e.g., pyroxenite veins) residing in a primarily depleted upper mantle [*Donnelly et al.*, 2004]. The formation of T-MORB magmas is commonly explained by either low extents melting of a depleted upper mantle and/or variable extents of mixing of an enriched mantle component (e.g., pyroxenite veins, plume component) with a depleted upper mantle source.

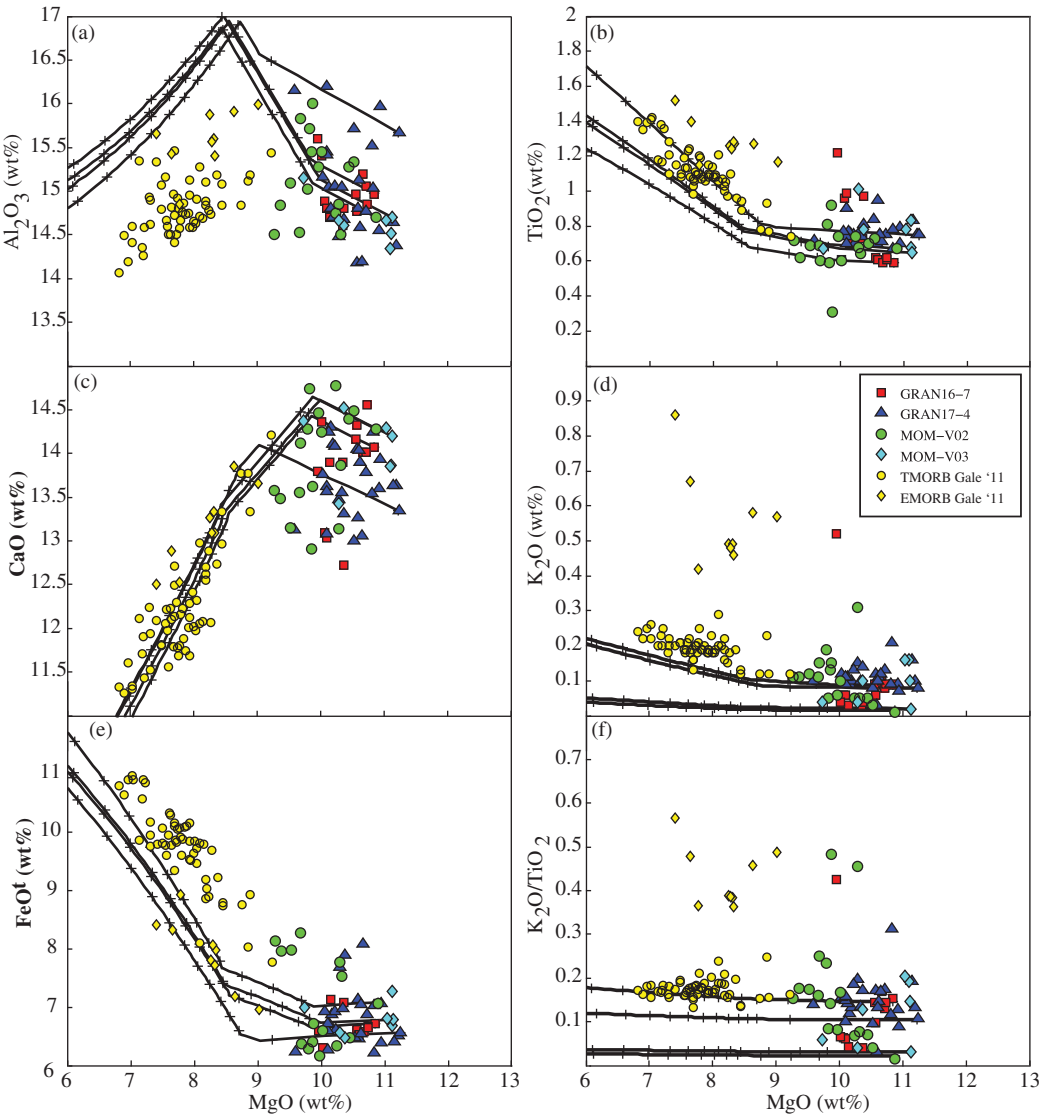

Figure 4. Major element concentrations of the Lucky Strike melt inclusions versus MgO (wt %). Compositions of glassy basalts erupted along the entire length of the segment are shown for comparison (yellow symbols) [*Gale et al*., 2011]. Fractional crystallization trends (calculated using PETROLOG) [*Danyushevsky and Plechov*, 2011] with relatively primitive melt inclusion compositions from each sample as starting compositions are shown as black lines, with tick marks at every 5% crystallization. The melt inclusion compositions require multiple parent magmas, are all more primitive than the basalt samples, and show little to no evidence of plagioclase crystallization.

Based on geochemical modeling, *Gale et al*. [2011] concluded that the Lucky Strike lavas cannot be formed by melting of a pyroxenite component and are instead produced from melting of a mantle that is composed of previously depleted upper mantle and low F Azores plume melts, plus or minus a regional Azores mantle component melted to greater extents. Specifically, *Gale et al*. [2011] suggest that the Lucky Strike E-MORB compositions formed from melting of a "metasomatized" mantle source that is produced from mixing of a previously depleted DMM mantle (with ~4 % melt extracted during an earlier melting event to account for the relatively depleted HREE compared to N-MORB) and low degree melts (F <3%) from the edges of the Azores plume generated within the garnet stability field (to account for the elevated highly incompatible elements and depleted HREE). This metasomatized mantle was then proposed to undergo 6–8% batch melting beneath Lucky Strike to produce the E-MORB lava compositions. *Gale et al*. [2011] suggested that the Lucky Strike T-MORB lavas were formed from melting of a heterogeneous mantle composed of 85% previously depleted mantle and 15% Azores mantle, along with the addition of low F melts from the edges of the Azores plume. Thus, two enriched components are required to account for elevated trace element ratios (Ba/La and La/Sm) in the Lucky Strike E- and T-MORB lavas [*Gale et al*., 2011].

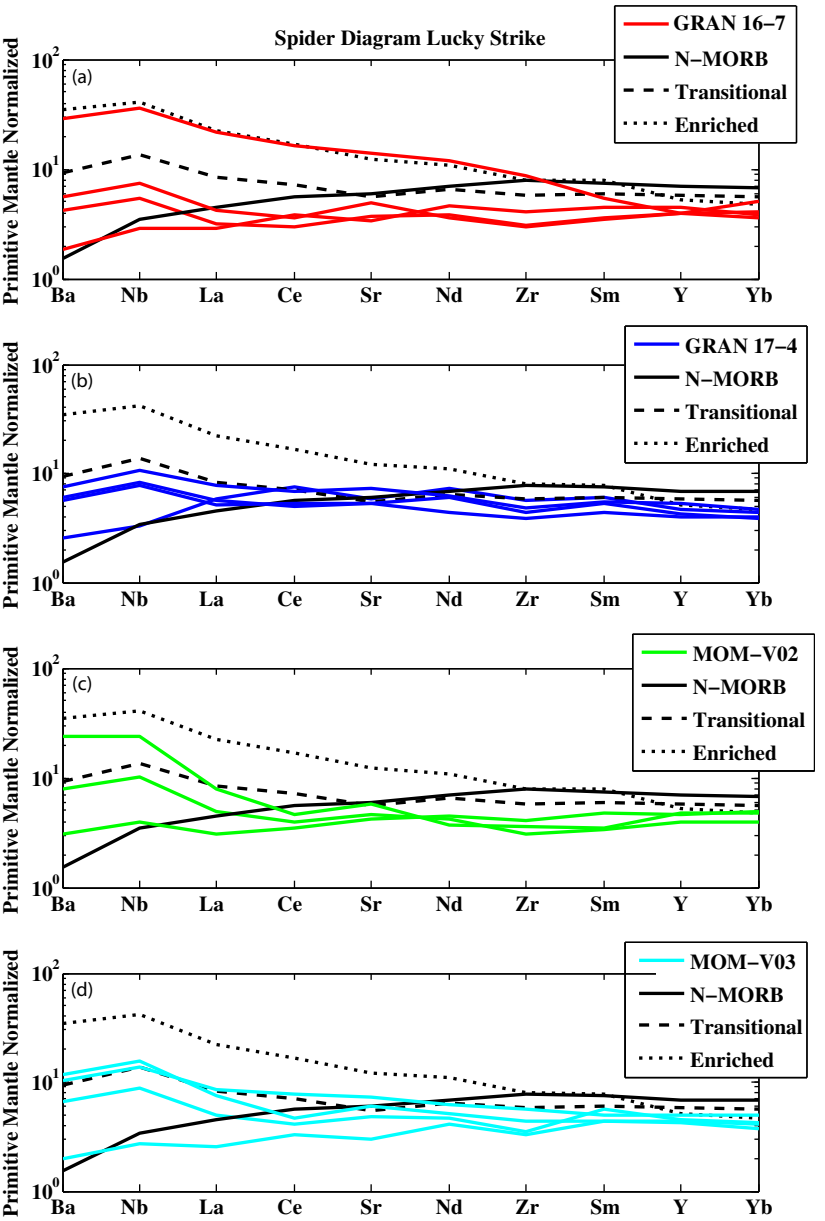

Figure 5. Primitive mantle normalized diagram [*McDonough and Sun*, 1995] of melt inclusions from each Lucky Strike sample. The average E-MORB and T-MORB compositions from Lucky Strike basalts [*Gale et al*., 2011] are shown as black-dotted and dashed lines, respectively. Although no N-MORB was sampled at Lucky Strike by *Gale et al*. [2011], we plot the average N-MORB of *Arevalo and McDonough* [2010] for comparison (solid black line). The melt inclusion compositions are similar to the E- and T-MORB lava compositions from *Gale et al*., [2011]. With the exception of the lone E-MORB melt inclusion (a), the range of MREE and HREE in the melt inclusions is relatively limited, but the LREE and highly incompatible elements are much more variable.

The presence of an Azores mantle component (either as low F melts or a regional component) beneath Lucky Strike is supported by numerical models suggesting that melts from the Azores plume may be deflected to the south due to asthenospheric flow caused by plate motion [*Yang et al*., 2006], and this deflection may also have a long-wavelength geophysical signature [e.g., *Cannat et al*., 1999*; Escartín et al*., 2001]. Low $^{21}Ne/^{22}Ne$ ratios for a given $^{20}Ne/^{22}Ne$ also indicate the presence of an Azores plume component; though, no plume signature is observed in He isotope ratios (R/Ra ranges from 8.19 to 8.56), which have values similar to Atlantic N-MORB [*Moreira et al*., 2011]. Although these geochemical models provide one possible explanation for the range of lava compositions erupted, it is difficult to physically explain how the relatively fertile low-F component from the Azores plume would be preserved and transport a few hundred kilometers along axis without being exhausted completely by adiabatic decompression melting

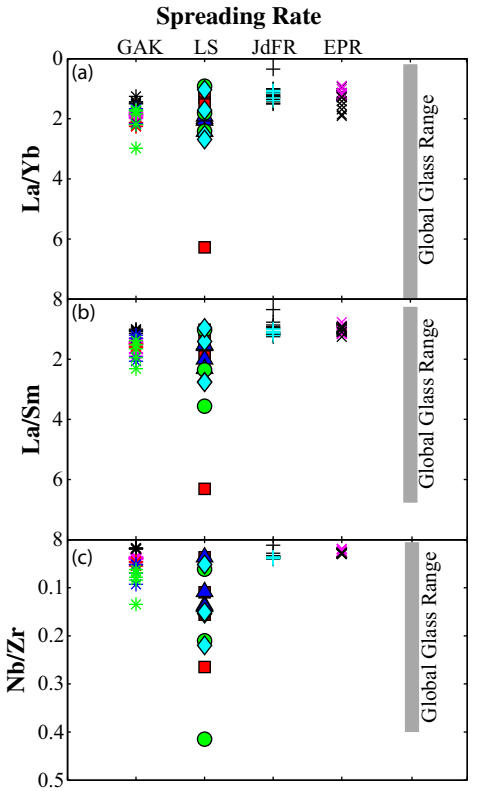

Figure 6. Trace element ratios of the Lucky Strike melt inclusions compared to melt inclusions from other MORs (GAK=Gakkel Ridge; *Shaw et al.* [2010]; *Wanless et al.* [2014]; JdFR=Juan de Fuca Ridge; *Wanless and Shaw* [2012]; and EPR = East Pacific Rise; *Wanless and Shaw* [2012]; LS=Lucky Strike, this study). Glass data for the global MOR system are shown as a gray bar [*Gale et al.*, 2013]. Samples from Lucky Strike were all collected within x km of each other but have a wider range of trace element ratios compared to samples collected various segments (different color symbols) of other MORs.

beneath the ridge segments north of Lucky Strike. Thus, to further investigate the source of the melt inclusion compositions at Lucky Strike, we modeled several different scenarios involving melting of a heterogeneous mantle beneath the Lucky Strike segment.

5.2. Trace Element Mantle Melting Models

We use a nonmodal, incremental, batch melting model to calculate the trace element composition of melts produced from a wide range of melting regime shapes, using a one-component or two-component mantle source, and considering various extents of melting [*Wanless et al.*, 2014]. We investigated cases in which melting occurs only in the spinel field, as well as cases involving melting that initiates in the garnet field and continues through the spinel field. An important aspect of this model is that it calculates the composition of melts produced from a spectrum of melting geometries, ranging from a full melting triangle to a single vertical column beneath the ridge axis (supporting information Figure S2). To do this, we systematically excluded increasing proportions of the outer edges ("wings") of the melting triangle in the calculation of the final pooled melt composition. Excluding these low degree "wing" melts in the final aggregate melt composition results in relatively depleted trace element compositions and elevated trace element ratios (e.g., Ba/La; La/Sm) compared to pooling of the entire melting regime [see *Wanless et al.*, 2014]. This model simulates inefficient transport of melt from the wings of the melting regime to the ridge axis as predicted by numerical models [e.g., *Ghods and Arkani-Hamed*, 2000; *Hebert and Montési*, 2011] and represents an alternative method for producing the relatively depleted MREE and HREE compositions observed in the Lucky Strike melt inclusions (Figure 5) and lavas [*Gale et al.*, 2011]. To simultaneously account for both the depleted HREE and the elevated incompatible elements, we evaluated the

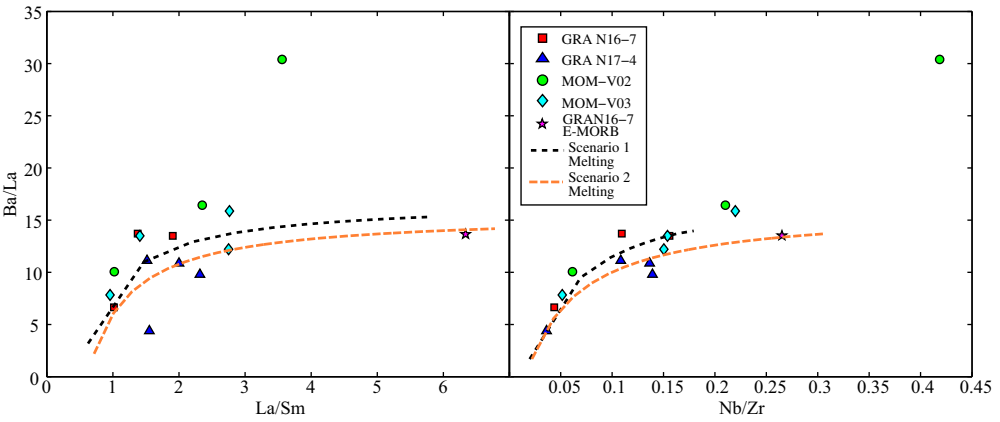

Figure 7. Comparison of trace element ratios of the Lucky Strike melt inclusions (filled symbols) and best-fit results from scenario 2 (orange dashed line) and scenario 1 (black dashed line) melting models. E-MORB compositions are best produced using scenario 2.

Table 5. Melting Reactions and Mantle Modes

	CPX	OPX	Olivine	Spinel	Garnet	Reference
Mantle modes						
Pyroxenite Mantle	82	0	0	0	18	Niu et al. [2007]
Lherzolite Mantle	13	28	57	2	0	Niu et al. [2007]
Depleted Mantle	5	20	73	1	1	Niu et al. [2007]
Melting reactions						
Pyroxenite	50	0	0	0	50	Kinzler [1997]
Spinel Reaction	97	25	−30	8	0	Kinzler [1997]
Garnet	100	−40	15	0	25	Longhi [2002]

composition of melts produced from various degrees of melting of a mantle consisting of different combinations of (1) depleted upper mantle [DMM; from *Workman and Hart*, 2005], (2) Azores mantle [AzM; *Gale et al*., 2011], and (3) pyroxenite veins [Px Vein; from *Donnelly et al*., 2004] for a spectrum of melting regime geometries. Because a regionally depleted mantle component has been invoked by previous studies [*Gale et al*., 2011], we also evaluated melting of a previously depleted upper mantle component [D-DMM; from *Workman and Hart*, 2005]. The D-DMM component is calculated in *Workman and Hart* [2005] by subtracting 2σ from the average DMM component determined by *Su and Langmuir* [2003]. Mantle modes and melting reactions are provided in Table 5 and partition coefficients used in the melting models are provided in *Wanless et al*. [2014].

In the simplest case—melting of a DMM or D-DMM-only mantle—we modeled triangular geometries with total extents of melting of 1, 3, 6, 9, 12, and 15%, where melts produced across the entire melting region are pooled in the final melt composition (top row of supporting information Figure S2). We calculated model compositions produced when the melting regime geometry is varied by progressively excluding melts produced in the wings of the melting triangle until melting occurs only in a vertical melting column beneath the ridge axis (lower rows in supporting information Figure S2). This results in 21 distinct melting regime shapes for DMM and D-DMM. For heterogeneous mantle compositions (DMM + AzM; DMM + PxVein; D-DMM + AzM; and D-DMM + PxVein), we used the same parameter space and assumed that either (1) the enriched component undergoes a fixed low extent of melting (F = 3%) compared to the depleted mantle component, or (2) that both components melt to the same extent. In Scenario 1, DMM or D-DMM melts produced from each of the 21 melting geometries were mixed (via binary mixing) with 3% melts from either AzM or PxVein in proportions from 0 to 100%. The low F melts from the enriched component are produced in the garnet stability field to account for major element concentrations of erupted lavas [*Gale et al*., 2011]. This scenario is similar to that invoked by *Gale et al*. [2011] to explain the E-MORB lavas erupted at Lucky Strike. Namely, low degree of melts generated within the garnet stability field on the edges of the Azores plume remelt and mix with melts generated from a regional upper mantle component that melts within the spinel stability field. In Scenario 2, we assumed that both mantle components melt to the same extent and the resulting melts from each component are mixed to form the final melt composition.

These melting calculations resulted in >800 theoretical melt compositions. To determine which melting parameters best account for the Lucky Strike compositions, we calculated the overall misfit for each modeled melt compared to the average N-MORB and T-MORB compositions (corrected to the host-olivine compositions) from each location, as well as the one E-MORB composition (GRA N16−7). The misfit value for each model composition was determined by subtracting the sum of the squares of the misfit of each element from the measured reference composition (see *Wanless et al*. [2014] for details). All trace elements presented in Figure 8 are used in misfit calculations and are weighted equally. An example misfit calculation for Sample GRA N16-7 is shown in supporting information Figure S5.

5.3. Formation of Lucky Strike Melt Inclusion Compositions

Theoretical melts produced using the previously depleted mantle source (D-DMM) result in a better fit compared to DMM for all melting scenarios, particularly with regard to the HREE compositions. This is consistent with the presence of a regionally depleted mantle hypothesized for the formation of E- and T-MORB lavas erupted along the Lucky Strike segment [*Gale et al*., 2011]. Therefore, we limit the following discussion to a mantle that includes a D-DMM component.

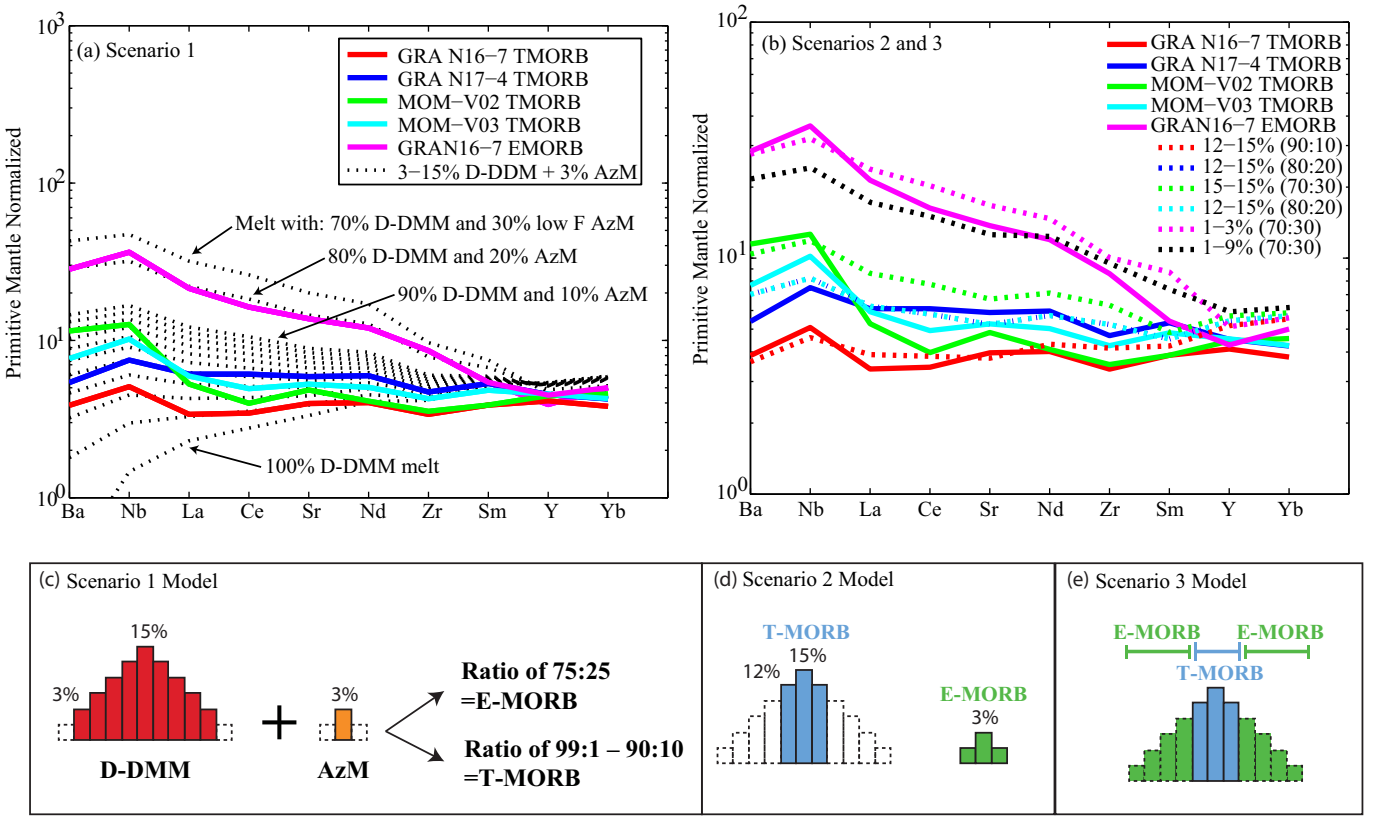

Figure 8. (a and b) Primitive mantle normalized diagram showing the Lucky Strike E-MORB and average T-MORB melt inclusion compositions (solid lines) and results of melting models (dashed lines). Melting parameters used in the best-fit melting models for (c) Scenario 1 and (d and e) Scenario 2. For Scenario 1 (Figure 8a), the best fit melting geometry is a low degree melt (3%) of Azores plume material plus pooling of 3–15% melting of D-DMM (Figure 8c). These mantle components are mixed at a ratio of 75% D-DMM to 25% low F AzM to produce the E-MORB compositions. Mixing of 90–99% D-DMM with 1–10% low F AzM to produce the T-MORB compositions (Figure 8c). Figure 8b Primitive mantle normalized diagram showing the best-fit melting models for each sample (dashed lines) and the average melt inclusion composition from each location (solid lines). The two blue-dashed lines overlap because best-fit models are the same for both samples. The range of T-MORB compositions can be produced by pooling of melts produced by melting of a heterogeneous mantle composed of both D-DMM and AzM in proportions ranging from 90–70% D-DMM to 10–30% AzM, but pooling over inner portions of the melting triangle (Scenario 2 and 3). E-MORB compositions can be produced from either smaller extents of melting (1–3%) of a mantle composed of 70% D-DMM and 30% AzM mantle (Figure 8d Scenario 2) or from pooling melts from the outer edges (1–9%) of the T-MORB melting triangle (black-dashed line in Figure 8e (Scenario 3).

Melting of a homogeneous mantle composed of D-DMM alone cannot produce the compositions observed in the Lucky Strike melt inclusions, suggesting that an enriched mantle component must be present (supporting information Figure S3). Of the two enriched mantle components investigated, the AzM source produced better fits to the data compared to the PxVein source. Using the pyroxenite vein as the second mantle component resulted in theoretical melts that were too enriched in MREE and HREE to explain the Lucky Strike melt inclusion compositions (supporting information Figure S4). Specifically, melting of the PxVein source produced ratios of LREE to MREE (e.g., La/Sm) that are too low and MREE to HREE (e.g., Sm/Yb) that are too high to explain the melt inclusion compositions. Thus, we favor a model that includes melting of an Azores plume component as opposed to pyroxenite veins, consistent with earlier trace element [*Gale et al.*, 2011], isotopic [*Moreira et al.*, 2011 and *Hamelin et al.*, 2013], and numerical modeling studies [*Yang et al.*, 2006] of the region. Below we discuss three possible melting scenarios that can explain the formation of the range of E-MORB to N-MORB melts observed in our Lucky Strike melt inclusions using a heterogeneous mantle composed of D-DMM and AzM.

Melting Scenario 1 assumes that the enriched and depleted mantle components melt to different degrees and the resulting melts are then mixed, while the Scenario 2 and 3 assume that both components melt to the same extent, but different total extents of melting are requited (Figure 8). For Scenario 1, D-DMM melts from all 21 melting geometries (shown in supporting information Figure S2) are mixed with a low F (3%) AzM melt. The best-fit parameters for this scenario require that the D-DMM melts produced in the outermost edges of the melting triangle are not pooled in the final melt composition (Figure 8c). Specifically,

trace element patterns most similar to Lucky Strike melt inclusion compositions are produced by pooling of melt from a region that includes 3–15% melts of D-DMM mixed with the low F (3%) melt from the AzM component (Figure 8a). The best-fit parameters for the range of average T-MORB and N-MORB compositions are produced by mixing of these two melt components in proportions of 90–99% D-DMM to 10–1% AzM. E-MORB compositions require a greater percentage of low F AzM (25%) compared to D-DMM (75%). Thus, varying the proportion of the low F AzM and the D-DMM in the final pooled melt can produce the range of melt inclusion compositions. One limitation of this model, however, is that the best-fit melt compositions cannot explain the Nb/Zr ratios greater than 0.20 observed in several Lucky Strike melt inclusions or the T-MORB melt inclusion with Ba/La values >30 (Figure 7).

In melting Scenario 2, both components (D-DMM and AzM) melt to the same extent and the resulting melts are then mixed in various proportions to form a range of theoretical melt compositions. In this scenario, the range of N-MORB and T-MORB compositions are produced from a single melting geometry and a heterogeneous mantle composed of two components. The proportions of the two components in the mantle source vary (Figure 8b). Specifically, N-MORB and T-MORB compositions are produced by pooling across a narrow melting region with 12–15% melt of a heterogeneous mantle composed of D-DMM and AzM (Figure 8d). To account for the range of T-MORB and N-MORB, the proportion of D-DMM to AzM varies from 70 to 90% D-DMM and 30 to 10% AzM. Lower total extents of melting are required to produce the trace element compositions of the E-MORB. For Scenario 2, the best-fit for the E-MORB composition requires 1–3% melting of a heterogeneous mantle composed of 70% D-DMM and 30% AzM (Figure 8d). Thus, the Lucky Strike melt inclusion compositions can be produced by varying the total extents of melting of a mantle composed of D-DMM and AzM. This result is similar to the modeling results for the formation of T-MORB lavas by *Gale et al*. [2011], but does not require the addition of a second enriched component (low-F melts and AzM component) to produce the trace element compositions. This melting scenario produces higher La/Sm and Nb/Zr ratios, but not higher Ba/La ratios (Figure 7) compared to Scenario one.

A variation of this melting model allows for concurrent formation of E-MORB to N-MORB using the same melting regime geometry and mantle source components (Scenario 3; Figure 8e). If the melting regime is triangular and the total extent of melting is 15%, the N-MORB compositions can be formed from pooling of the inner portion (12–15%) of the melting triangle, as described above in Scenario 2, while E-MORB compositions can be formed by pooling only the outer edges of this melting regime (1–9% melts) (Figure 8e). This model implies that E-MORB compositions are formed continuously at the outer edges of the melting triangle beneath Lucky Strike, but may not always be transported, preserved, and erupted at the surface. This suggests two possible models in which the E-MORB compositions form without the presence of low F melts; either (1) simultaneously with the N-MORB by pooling different regions of the same melting triangle (Figure 8e), or (2) during periods of lower magma supply (and thus shorter melting columns), when N-MORB compositions are not produced (Figure 8d). Despite calculating >800 theoretical melt compositions using a range of melting geometries and mantle source compositions, the low La concentrations in the melt inclusions are not produced. Low La concentrations contribute to the elevated Ba/La ratios, which are also difficult to reproduce with the melting models. This may reflect errors in partition coefficients used, melting reactions assumed in the modeling, or mantle source compositions that have been proposed.

6. Discussion

6.1. Mantle Melting and Source Composition

In contrast to previous studies [*Gale et al*., 2011] that require three different mantle components to account for the E- and T-MORB lava compositions (D-DMM + Low F melts=E-MORB and D-DMM + AzM + Low F melts=T-MORB), our modeling suggests that E-MORB, T-MORB, and N-MORB melt inclusion compositions only require two mantle components. Although our results are consistent with geochemical evidence and numerical modeling that suggest the Lucky Strike mantle is contaminated by the plume component [*Yang et al*., 2006; *Moreira et al*., 2011; *Hamelin et al*., 2013], we show that this contaminant does not need to consist of both low degree AzM melts and a regional AzM component.

Our trace element melting models result in three plausible scenarios for the formation of melt inclusion compositions at Lucky Strike (Figure 8). Trace element concentrations and ratios in Scenarios 2 and 3 that use only the regional AzM component (Figures 8d and 8e) provide quantitatively better fits to the Lucky

Table 6. Example of Results From Melting Models[a]

	GRAN16-7avg	Scenario 1 Best Fit	Scenario 2 Best Fit
Ba	25.5	12.2	24.1
Nb	3.3	2.1	3.1
La	2.2	2.3	2.6
Ce	5.8	6.6	6.7
Sr	79.0	86.6	78.2
Nd	5.0	6.3	5.7
Zr	35.5	48.5	41.2
Sm	1.6	2.3	1.8
Y	17.7	21.6	20.7
Yb	1.7	2.4	2.1

	GRAN16-7 EMORB	Scenario 1 Best Fit	Scenario 2 Best Fit	Scenario 3 Best Fit
Ba	187	180	182	184
Nb	24	20	21	20
La	14	14	15	14
Ce	27	30	34	31
Sr	273	284	333	309
Nd	15	16	18	19
Zr	90	83	106	107
Sm	2	2.9	3.5	3.4
Y	17	20	22	25
Yb	2.2	2.1	2.5	2.7

[a]All concentrations in ppm.

Strike trace element ratios compared to trace element concentrations produced in Scenario 1 (Figure 8c), which requires the low F component (Table 6). In both Scenarios 2 and 3, slight variations in the proportion of the AzM component and changes in the total extent of melting (possibly reflected in waxing and waning magma supply or separate regions of melt pooling) accounts for the range of melt inclusion compositions observed. However, the low total extents of melting required to produce the E-MORB compositions (3%) in Scenario 2 will not produce major element compositions of a tholeiitic basalt, suggesting that this scenario (Figure 8d) is not appropriate for the formation of Lucky Strike E-MORB compositions. Instead, the higher total extents of melting for E-MORB (9%) in Scenario 3 are more appropriate. The variability in the total extents of melting beneath Lucky Strike may result from temporal fluctuations in the magma supply. Thus, T-MORB are formed during periods of enhanced magmatism at Lucky Strike, while E-MORB formed during periods of lower magma supply. A waxing and waning magma supply is consistent with geophysical studies that show fluctuations in crustal thickness in the off-axis crust adjacent to Lucky Strike [*Cannat et al.,* 1999*; Escartín et al.,* 2001*; Seher et al*., 2010].

It is possible that three components are involved in melting beneath Lucky Strike, as was suggested based on trace element systematics and radiogenic isotopes of erupted lavas [*Gale et al*., 2011]. These authors argue that the Lucky Strike lavas have a second enriched component that is distinct from the regional gradient in the AzM component with distance south of the Azores Plume. They attribute this enriched signature to metasomatism of the Lucky Strike mantle with low F melts from the edges of the Azores plume. Our data can be reconciled with these observations if E-MORB compositions form from the combination of low F melts and D-DMM (Scenario 1) and the N-MORB and T-MORB form from Scenario 3. Although it is not difficult to envision how this fertile low F component may form in the mantle, it seems difficult to imagine how it would be preserved and erupted at Lucky Strike, and is not completely exhausted at segments KP-2, KP-3, KP-4, and Menez Gwen that lie between Lucky Strike and the Azores. For this reason, we prefer a model that does not require a low F component to produce the melt inclusion compositions at Lucky Strike (as envisioned in either the three-component *Gale et al*. [2011] model or our Scenario 1).

Rather, our preferred model for the range of trace element compositions at Lucky Strike is Scenario 3, where T-MORB and N-MORBs are formed in the central portion of the melt triangle beneath the ridge axis, while the E-MORB melts are formed at the edges of the melting triangle, but are not always erupted at the ridge axis. This model is motivated by the observed temporal variability in magma supply suggested for the Lucky Strike segment [*Seher et al*., 2010; *Escartín et al.,* 2014]. We hypothesize that the E-MORB melts are less likely to be extracted (or preserved) during periods of elevated magma supply when the system is overwhelmed by melts with higher total extents of melting. Instead, they are more likely to be preserved and erupted during periods of lower magma supply when there is less magma fluxing through the system. Thus, E-MORB may erupt at the beginning or end of an eruptive cycle at Lucky Strike; between these eruption, N-MORB and T-MORB compositions dominate the system.

6.2. Depths of Crystallization

Based on vapor saturation pressures, melt inclusion entrapment at the Lucky Strike segment occurs from below the crust-mantle transition (>9 km bsf) upward through to shallow crustal levels (Figure 2). If all 64

melt inclusions are considered together (Figure 3a), the peak in crystallization depths (>45% of the melt inclusions) is consistent with the geophysically determined melt lens top at ~3.4 km bsf [*Singh et al*., 2006]. When each lava sample is considered individually (Figures 3b–3e), the percentage of melt inclusions entrapped at a given depth varies, but at all four locations ≥35% of the melt inclusions have pressures consistent with crystallization in the melt lens. Approximately 20% of melt inclusions have crystallization depths shallower than the seismically imaged melt lens, indicating crystallization during ascent from the melt lens to the seafloor. The pronounced peak in crystallization depths at ~1–2.5 km bsf in sample GRA N17-4 (Figure 3c), which was erupted along the axis on the north flank of the volcano (Figure 1), may reflect crystallization during lateral transport in shallow dikes. However, these shallow signatures may also result from degassing or reequilibration of the melt inclusion volatiles during ascent to the seafloor.

Furthermore, 15–50% of the melt inclusions form below the melt lens, in the lower crust, at all four locations (~30% when all melt inclusions are considered together; Figure 3a). This observation is inconsistent with accretion models that build the oceanic crust solely from the melt lens down (e.g., gabbro glacier models; [*Nicolas and Reuber*, 1988; *Quick and Denlinger*, 1993]) and favors a model of distributed crustal accretion [e.g., *Kelemen et al*., 1997; *Korenaga and Kelemen*, 1997; *Kelemen and Aharonov*, 1998] consistent with previous melt inclusion studies at fast-spreading and intermediate-spreading ridges [*Wanless and Shaw*, 2012]. Accretion in the lower crust is also consistent with the observed low-velocity zone in the lower crust at Lucky Strike, beneath the seismically imaged melt lens [*Seher et al*., 2010]. While this low-velocity signature may result from elevated crustal temperatures, the preferred interpretation is that this zone is composed of <1% remnant melt that occupies the pathway of melt delivery from the mantle to the shallow melt lens [*Seher et al*., 2010]. Therefore, olivine crystallization below the melt lens may occur either as a result of cooling as melts stall in the lower oceanic crust or from melts crystallizing during ascent from the mantle to the melt lens via porous flow. However, the relatively primitive nature of the melt inclusions and host-olivine suggests that stalled melts are not highly evolved. Regardless, the entrapment pressures observed at Lucky Strike favor a model of distributed accretion, which may suggest a similar mode of accretion along other slow-spreading ridge segments with a shallow melt lens.

6.3. Fractional Crystallization in Mantle and Crust

Relatively primitive mantle melts may be influenced by a number of petrologic processes that occur during extraction from the melting region, during ascent through the mantle or oceanic crust, and/or during storage within the melt lens. Evidence of these processes can be preserved in the composition of the melt inclusions and host-olivines. For example, basaltic melts that cool and differentiate at crustal pressures beneath MORs will typically undergo olivine crystallization followed by olivine + plagioclase (+/- clinopyroxene). To assess the evolution of melts within the Lucky Strike magmatic system, we examined compositional trends as a function of crystallization depth determined from CO_2-H_2O saturation pressures from the four locations (Figures 9 and 10). Increasing extents of olivine crystallization during ascent is inferred in samples MOM-V02 and GRA N17-4 based on Al_2O_3 and H_2O variations as a function of pressure (Figure 9). Specifically, sample GRA N17-4 shows increasing H_2O and Al_2O_3 concentrations with decreasing depth, suggesting increasing degrees of olivine crystallization as the melt ascends from the mantle and crystallize in the melt lens. However, MgO concentrations do not decrease significantly with depth and two samples (GRA N16-7 and MOM-V03) show no systematic trend of increasing degrees of olivine crystallization with decreasing depth (Figure 9), indicating that some melts ascend from the mantle through the lower crust to the melt lens/seafloor without undergoing significant differentiation.

Increasing Al_2O_3 concentrations with decreasing MgO (Figure 4) and small positive Sr anomalies (compared to elements of similar incompatibilities) in mantle-normalized diagrams (Figure 5) suggest that there is little plagioclase crystallization prior to melt entrapment. This is supported by the petrologic models of fractional crystallization that predict the onset of plagioclase crystallization in the Lucky Strike melts only after they have evolved beyond 8.7 wt % MgO (Figure 4). Instead, the range of major element concentrations in the melt inclusions can be best explained by ~10% olivine-only crystallization from numerous parental melts (Figure 4). By contrast, the magmas that produced the basaltic glasses erupted along the Lucky Strike segment have likely experienced both olivine and plagioclase crystallization [*Gale et al*., 2011].

Numerous studies have proposed that ascending melts are chemically altered during ascent through the mantle to the base of the crust. For example, at the EPR and JdFR, olivines entering the base of the crust

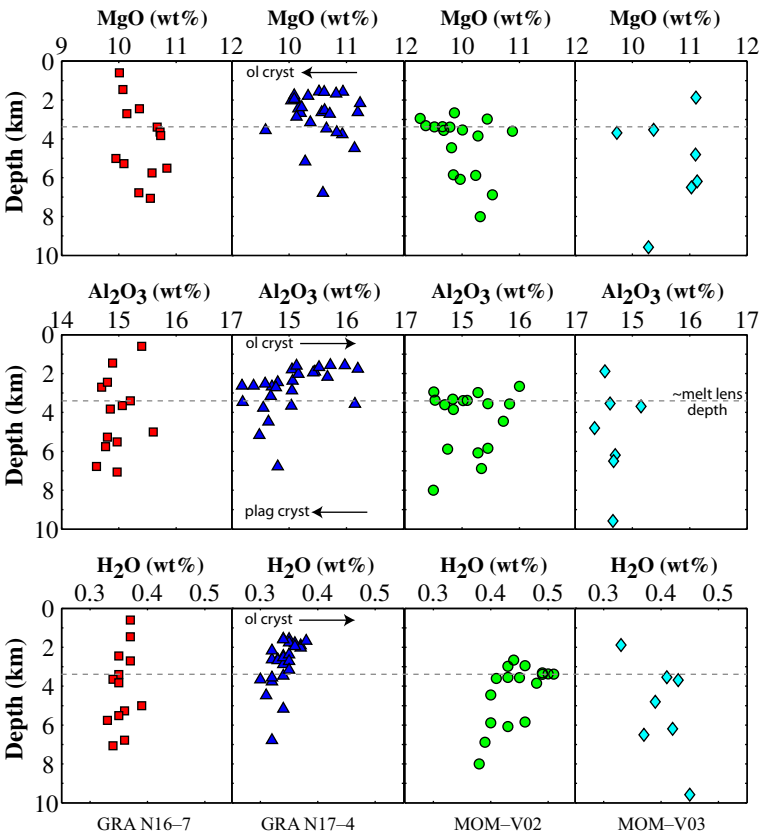

Figure 9. Major element compositions versus depth of entrapment (km below seafloor; bsf). The approximate depth of the melt lens (at ~ 3.4 km; *Singh et al*., 2006] is shown as a gray-dashed line. The most primitive compositions (high MgO, low H_2O) are observed at all depths within the ocean crust. Significant melt differentiation is observed at melt lens depths in sample MOM-V02 (green circles) and GRA N17-4 (blue triangles); however, is less consistent in other melt inclusion compositions.

have maximum Mg#'s of 87 (compared to Mg#'s $\geq$ 90 that are in equilibrium with mantle), indicating that some olivine crystallization occurred in the mantle [*Wanless and Shaw*, 2012]. By contrast, olivines erupted at Lucky Strike are remarkably primitive, with over 90% of the phenocrysts having Mg#'s of 89–92 (Table 3). This suggests that melts entering the base of the crust at Lucky Strike are relatively primitive and that significant olivine crystallization has not occurred in the mantle. Thus, despite the fact that some crystallization must occur and is concentrated in the vicinity of the melt lens, (Figure 3), the primitive host-olivine and limited extents of fractional crystallization (i.e., olivine only) recorded by the melt inclusions indicate limited magma differentiation prior to entrapment, suggesting limited melt residence times within the crust.

The relatively primitive nature of the Lucky Strike melt inclusions and host-olivine allow us to estimate the pressures and temperatures of the primary mantle melts. A thermobarometer developed by *Lee et al*., [2009] is appropriate for calculating primary magma characteristics because the Lucky Strike melt inclusions show little to no plagioclase saturation and we have eliminated pyroxenite vein as a possible mantle source. Using a Fe^{3+}/Fe^{T}=0.15 appropriate for mid-ocean ridges [*Kelley and Cottrell*, 2009] and olivine forsterite contents of 0.91 (consistent with our host-olivine compositions; Table 3), melt inclusions have primary magma temperatures ranging from ~1215 to 1340°C and average pressures of melting that range from 0.6 to 1 GPa (20–35 km). These melting temperatures and pressures are similar to estimates from melt inclusions compositions collected at the FAMOUS segment of the MAR [*Laubier et al*., 2007], which suggests that melting temperatures and pressures are similar despite the notion that the Lucky Strike segment is more magmatically robust compared to other segments along the MAR. These depths are consistent with melting predominately occurring in the spinel stability field, which is consistent with our trace element models. However, it does not preclude small extents of melting in the presence of garnet (>60 km), as is suggested for the low F Lucky Strike melts [*Gale et al*., 2011]. The Lucky Strike melt inclusions plot on a higher geotherm (shallower, hotter melting) compared to melt inclusions from the ultraslow-spreading Gakkel Ridge

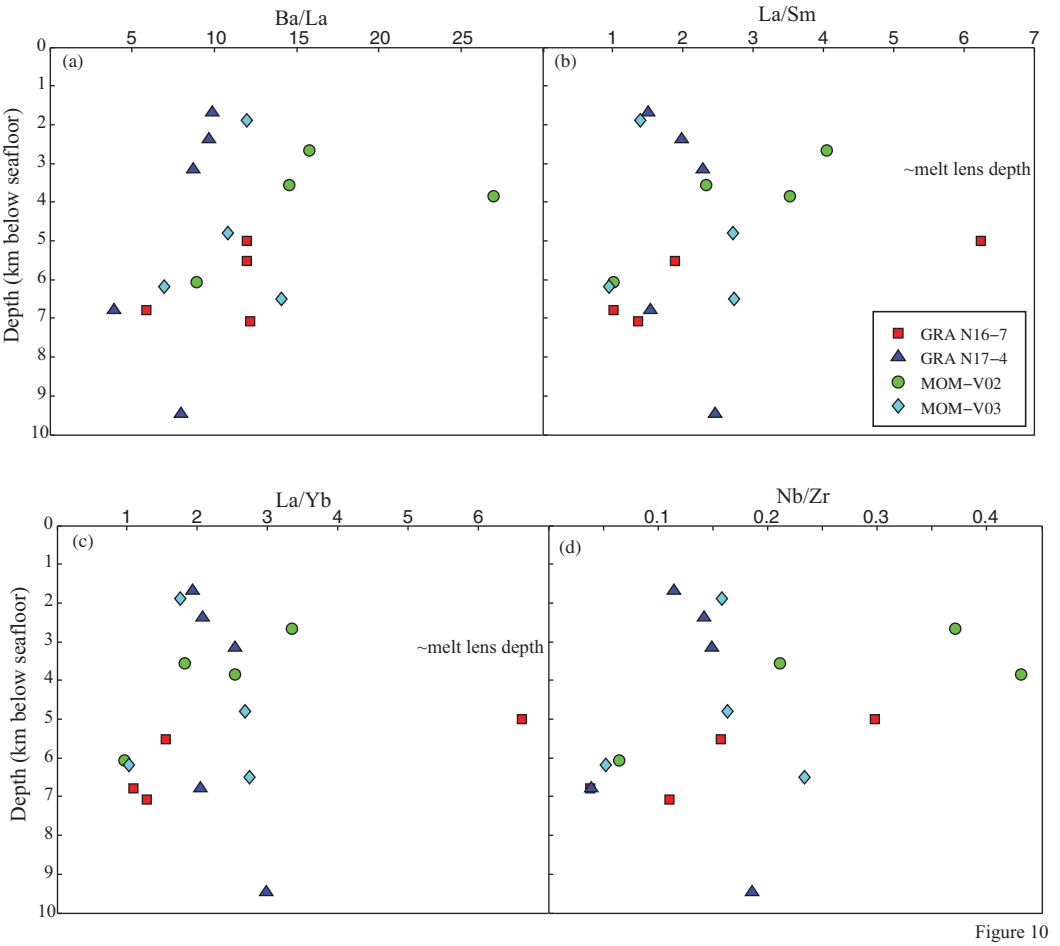

Figure 10

Figure 10. Trace element ratios of the Lucky Strike melt inclusions versus depth (in km bsf). The melt inclusions have a wide range of trace element ratios at all depths within the crust and mantle, suggesting that there is no region of significant melt homogenization at slow-spreading ridges.

[*Shaw et al.*, 2010], which is consistent with a faster spreading rate at the slow-spreading MAR compared to Gakkel Ridge. If olivine forsterite contents of 0.90 [*Lee et al.*, 2009] are used instead of 0.91, melting temperatures and pressures shift to lower values (1200–1300°C and 0.25 to 0.85 GPa).

6.4. Role of the Melt Lens at Lucky Strike

The presence of a quasi steady state melt lens beneath fast-spreading and intermediate-spreading ridges is thought to reflect a region where melts repeatedly pool, crystallize, erupt, and are replenished, resulting in lava compositions that are more evolved, but relatively limited in trace element and isotopic ratios [*Rubin et al.*, 2009]. By contrast, lavas erupted at slower-spreading ridges, where a steady state melt lens is typically absent [*Detrick et al.*, 1990], are generally found to be more primitive and have greater trace element variability [*Bonatti et al.*, 2003]. This results in little to no melt differentiation or homogenization beneath slow-spreading ridges and indicates shorter magma residence times in the shallow magmatic plumbing system [*Rubin et al.*, 2009].

We find that the Lucky Strike melt inclusion compositions are more primitive (higher Mg# host-olivine) and have higher trace element variability compared to melt inclusions from fast-spreading and intermediate-spreading centers [*Wanless and Shaw*, 2012] (Figure 6), but that the overall distributions of crystallization depths are similar (Figure 11). This implies that the Lucky Strike melt lens is a region of significant crystallization, but that it is not a region where extensive magma mixing or homogenization occurs. The wide range of trace element ratios observed at all depths within the crust suggests that melts are not homogenized anywhere within the Lucky Strike magmatic system (Figure 10), despite the presence of a shallow melt lens

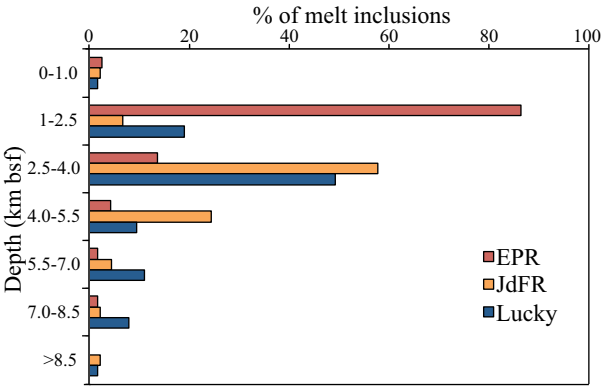

Figure 11. Histogram comparing the distribution of crystallization in the oceanic crust/mantle for the Lucky Strike melt inclusions (blue), EPR melt inclusions (red), and JdFR melt inclusions (orange). The peak in crystallization at all three spreading centers occurs in the shallow crust, at or near the seismically imaged melt lens. Greater than 20% of melt inclusions at all three ridges crystallize at depths below then the melt lens.

at the present time. While the imaged melt lens may be transient, the evidence of melt concentration at the segment center and the presence of different phases of significant volcanism [*Escartín et al*., 2014] likely fed by one or several subsequent AMCs. This is markedly different than the range of trace element compositions observed in olivine-hosted melt inclusions from fast-spreading and intermediate-spreading ridges [*Wanless and Shaw*, 2012], but it is similar to melt inclusion compositions from other slow-spreading MAR segments, where there is no geophysical evidence of a melt lens at the present time [*Shimizu*, 1998; *Laubier et al*., 2007, 2012]. This suggests that while the shallow melt lens at Lucky Strike may be atypical for slow-spreading ridge environments, the deeper magmatic system (melting geometry, mantle heterogeneity, and melt extraction processes) produces melt compositions that are similar to other slow-spreading ridge segments without melt lenses.

Trace element ratios in the Lucky Strike melt inclusions are also more variable than melt inclusions from the entire length of the Eastern Volcanic Zone on the ultraslow-spreading Gakkel Ridge (Figure 6). At Gakkel Ridge, melts are likely homogenized along-axis in the mantle beneath individual large volcanic centers, commonly resulting in a relatively limited range of trace element ratios at a given volcanic center [*Wanless et al*., 2014]. At Lucky Strike, there is geophysical evidence of focused upwelling and magmatism at the segment center [*Detrick et al*., 1995; *Thibaud et al*., 1998; *Cannat et al*., 1999; *Seher et al*., 2010]; however, there is no geochemical evidence of melts being homogenized beneath the Lucky Strike volcano. We suggest that this would require an AMC that is highly crystalline, and where melt is stored without efficient mixing.

Thus, in summary, the lack of melt homogenization, high Mg# of the host-olivine, and the absence of significant melt differentiation beyond olivine crystallization (Figure 9) suggests inefficient melt pooling and relatively short melt residence times of magmas in the crust/melt lens beneath Lucky Strike.

7. Conclusions

The Lucky Strike melt inclusions display a wide range of compositions ranging from E- MORB to N-MORB. To evaluate the source of melt inclusions, we modeled melting of a heterogeneous mantle using a nonmodal, incremental, batch-melting model that calculates the composition of melts produced from a wide range of melting regime shapes and various extents of melting. We compared over 800 melt compositions produced from 21 melting geometries using four mantle source components (DMM, D-DMM, Pyroxenite Veins and Azores Mantle) to determine the melt parameters that best explained the range of melt inclusion compositions observed. E-MORB to N-MORB compositions can be formed from melting of a heterogeneous mantle composed of D-DMM and Azores Mantle, where both components melt to the same extent and the compositional variations are produced by slight differences in (1) the proportion of the Azores plume component, and (2) the total extent of melting. Specifically, the range of N-MORB and T-MORB compositions are produced by a total of 15% melting, where melts from only the inner portions of the melting regime are pooled (12–15%). Varying the proportion of the AzM component compared to D-DMM in the starting source accounts for the range N-MORB and T-MORB compositions. By contrast, the E-MORB compositions can be formed either by lower total extents of melting (1–3%) of the same AzM mantle source during periods of decreased magmatism or by pooling melts from the outer edges of the same melting regime that forms the N-MORB compositions. However, it is difficult to produce the tholeiitic major element

compositions of the E-MORB with only 1–3% melting, and thus, we prefer a model where the E-MORB are formed on the outer edges of the melting triangle.

The distribution of crystallization based on volatile concentrations in melt inclusions at Lucky Strike is similar to that observed at the faster spreading EPR and JdFR—with the greatest percentage of crystallization in or near the melt lens, and a significant proportion of crystallization occurring beneath the melt lens in the lower crust. This indicates that the melt lens is an important region of crystallization at all spreading rates. However, the Mg#'s of the Lucky Strike host-olivine are relatively primitive, suggesting little to no melt differentiation prior to entrapment in the phenocryst and there is no evidence of extensive crystallization based on major element concentrations. Moreover, in contrast to the EPR and JdFR, the observed trace element variability in the Lucky Strike melt inclusions suggests that the melts are not homogenized within the magmatic plumbing system, despite the presence of a crustal melt lens. Thus, the lack of melt homogenization, the high Mg# of the host-olivine, and the absence of significant melt differentiation beyond olivine crystallization in the Lucky Strike melt inclusions suggests there is no region of melt homogenization within the system and that the melt residence times in the crust/melt lens at Lucky Strike is relatively limited.

Acknowledgments

We thank B. Monteleone at the WHOI ion microprobe facility, R. Hervick and L. Williams at ASU ion microprobe facility, and N. Chatterjee at the MIT electron microprobe facility for their analytical assistance. G. Toltin is thanked for his help with sample preparation. The GRAVILUCK'06 and Bathyluck'08 cruises where financed by the French Ministry of Research. This work was supported by NSF grant OCE-0926422 to A.M.S., OCE-PRF-1226130 to V.D.W., OCE-1333492 to S.A.S., and EAR-09-48666 to M.D.B., and by ANR (France) Mothseim Project NT05-342213 to J.E. Data for the figures are available in Tables 1–4 and supporting information Tables S1–S3 and will be made available through PetDB.

References

Arevalo, R., and W. F. McDonough (2010), Chemical variations and regional diversity observed in MORB, *Chem. Geol.*, *271*, 70–85.

Arnulf, A. F., A. J. Harding, S. C. Singh, G. M. Kent, and W. C. Crawford (2014), Nature of upper crust beneath the Lucky Strike volcano using elastic full waveform inversion of streamer data, *Geophys. J. Int.*, *196*(3), 1471–1491, doi:10.1093/gji/ggt461.

Barreyre, T., J. Escartín, R. Garcia, M. Cannat, E. Mittelstaedt, and R. Prados (2012), Structure, temporal evolution, and heat flux estimates from the Lucky Strike deep-sea hydrothermal field derived from seafloor image mosaics, *Geochem. Geophys. Geosyst.*, *13*, Q04007, doi:10.1029/2011GC003990.

Bonatti, E., M. Ligi, D. Brunelli, A. Cipriani, P. Fabretti, V. Ferrante, L. Gasperini, and L. Ottolini (2003), Mantle thermal pulses below the Mid-Atlantic Ridge and temporal variations in the formation of oceanic lithosphere, *Nature*, *423*(6939), 499–505, doi:10.1038/nature01594.

Calvert, A. J. (1997), Backscattered coherent noise and seismic reflection imaging of the oceanic crust: An example from the rift valley of the Mid-Atlantic Ridge at 23°N, *J. Geophys. Res.*, *102*(B3), 5119–5133, doi:10.1029/96JB03798.

Cannat, M., A. Briais, C. Deplus, and J. Escartín (1999), Mid-Atlantic Ridge–Azores hotspot interactions: Along-axis migration of a hotspot-derived event of enhanced magmatism 10 to 4 Ma ago, *Earth Planet. Sci. Lett.*, *173*, 257–269.

Crawford, W. C., A. Rai, S. C. Singh, and M. Cannat (2013), Hydrothermal seismicity beneath the summit of Lucky Strike volcano, Mid-Atlantic Ridge, *Earth Planet. Sci. Lett.*, *373*, 118–128.

Danyushevsky, L. V. (2002), Melt inclusions in olivine phenocrysts: Using diffusive re-equilibration to determine the cooling history of a crystal, with implications for the origin of olivine-phyric volcanic rocks, *J. Petrol.*, *43*(9), 1651–1671, doi:10.1093/petrology/43.9.1651.

Danyushevsky, L. V., and P. Plechov (2011), Petrolog3: Integrated software for modeling crystallization processes, *Geochem. Geophys. Geosyst.*, *12*, Q07021, doi:10.1029/2011GC003516.

Detrick, R. S., J. C. Mutter, P. Buhl, and I. I. Kim (1990), No evidence from multichannel reflection data for a crustal magma chamber in the MARK area on the Mid-Atlantic Ridge, *Nature*, *347*(6288), 61–64, doi:10.1038/347061a0.

Detrick, R. S., H. D. Needham, and V. Renard (1995), Gravity anomalies and crustal thickness variations along the Mid-Atlantic Ridge between 33°N and 40°N, *J. Geophys. Res.*, *100*(B3), 3767–3787, doi:10.1029/94JB02649.

Dixon, J. E., E. M. Stolper, and J. Holloway (1995), An experimental study of water and carbon dioxide solubilities in mid-ocean ridge basaltic liquids. Part I: Calibration and solubility models, *J. Petrol.*, *36*(6), 1607–1631.

Donnelly, K., S. Goldstein, C. Langmuir, and M. Spiegelman (2004), Origin of enriched ocean ridge basalts and implications for mantle dynamics, *Earth Planet. Sci. Lett.*, *226*(3-4), 347–366.

Dusunur, D., J. Escartín, V. Combier, T. Seher, W. Crawford, M. Cannat, S. C. Singh, L. M. Matias, and J. M. Miranda (2009), Seismological constraints on the thermal structure along the Lucky Strike segment (Mid-Atlantic Ridge) and interaction of tectonic and magmatic processes around the magma chamber, *Mar. Geophys. Res.*, *30*(2), 105–120, doi:10.1007/s11001-009-9071-3.

Escartín, J., M. Cannat, and G. Pouliquen (2001), Crustal thickness of V-shaped ridges south of the Azores: Interaction of the Mid-Atlantic Ridge (36°–39°N) and the Azores hot spot, *J. Geophys. Res.*, *106*(B10), 21,719–21,735, doi:10.1029/2001JB000224.

Escartín, J., S. A. Soule, M. Cannat, D. J. Fornari, D. Düşünür, and R. Garcia (2014), Lucky Strike seamount: Implications for the emplacement and rifting of segment-centered volcanoes at slow spreading mid-ocean ridges, *Geochem. Geophys. Geosyst.*, *15*, 4157–4179, doi:10.1002/2014GC005477.

Fouquet, Y., J.-P. Eissen, H. Ondreas, F. Barriga, R. Batiza, and L. Danyushevsky (1998), Extensive volcaniclastic deposits at the Mid-Atlantic Ridge axis: Results of deep-water basaltic explosive volcanic activity? *Terra Nova*, *10*(5), 280–286, doi:10.1046/j.1365-3121.1998.00204.x.

Gale, A., S. Escrig, E. J. Gier, C. H. Langmuir, and S. L. Goldstein (2011), Enriched basalts at segment centers: The Lucky Strike (37 17′ N) and Menez Gwen (37 50′ N) segments of the Mid-Atlantic Ridge, *Geochem. Geophys. Geosyst.*, *12*, Q06016, doi:10.1029/2010GC003446.

Gale, A., C. A. Dalton, C. H. Langmuir, Y. Su, and J.-G. Schilling (2013), The mean composition of ocean ridge basalts, *Geochem. Geophys. Geosyst.*, *14*, 489–518, doi:10.1029/2012GC004334.

Ghods, A., and J. Arkani-Hamed (2000), Melt migration beneath mid-ocean ridges, *Geophys. J. Int.*, *140*, 687–697.

Hamelin, C., A. Bézos, L. Dosso, J. Escartín, and M. Cannat (2013), Atypically depleted upper mantle component revealed by Hf isotopes at Lucky Strike segment, *Chem. Geol.*, *341*, 128–139.

Hauri, E., J. Wang, J. Dixon, P. King, C. Mandeville, and S. Newman (2002), SIMS analysis of volatiles in silicate glasses: 1. Calibration, matrix effects and comparisons with FTIR, *Chem. Geol.*, *183*(1–4), 99–114.

Hebert, L. B., and L. Montési (2011), Melt extraction pathways at segmented oceanic ridges: Application to the East Pacific Rise at the Siqueiros transform, *Geophys. Res. Lett.*, *38*, L11306, doi:10.1029/2011GL047206.

Humphris, S. E., D. J. Fornari, D. S. Scheirer, C. R. German, and L. M. Parson (2002), Geotectonic setting of hydrothermal activity on the summit of Lucky Strike Seamount (37°17′N, Mid-Atlantic Ridge), *Geochem. Geophys. Geosyst.*, *3*(8), 1049, doi:10.1029/2001GC000284.
Izenman, A. (1991), Recent developments in nonparametric density estimation, *J. Am. Stat. Assoc.*, *86*, 205–224.
Katz, R. F., and S. M. Weatherley (2012), Consequences of mantle heterogeneity for melt extraction at mid-ocean ridges, *Earth Planet. Sci. Lett.*, *335–336*, 226–237, doi:10.1016/j.epsl.2012.04.042.
Kelemen, P. B. and E. Aharonov (1998), Periodic formation of magma fractures and generation of layered gabbros in the lower crust beneath oceanic spreading ridges, in *Faulting and Magmatism at Mid-Ocean Ridges, AGU Monogr.* vol. 106, edited by W. Roger Buck et al., pp. 267–289, AGU, Washington, D. C.
Kelemen, P. B., N. Shimizu, and V. J. M. Salters (1995), Extraction of mid-ocean-ridge basalt from the upwelling mantle by focused flow of melt in dunite channels, *Nature*, *375*(6534), 747–753, doi:10.1038/375747a0.
Kelemen, P., G. Hirth, N. Shimizu, M. Spiegelman, and H. Dick (1997), A review of melt migration processes in the adiabatically upwelling mantle beneath oceanic spreading ridges, *Philos. Trans. Math. Phys. Eng.Sci.*, *355*(1723), 283–318.
Kelley, K., and E. Cottrell (2009), Water and the oxidation state of subduction zone magmas, *Science*, *325*, 605–607.
Kinzler, R. J. (1997), Melting of mantle peridotite at pressures approaching the spinel to garnet transition: Application to mid-ocean ridge basalt petrogenesis, *J. Geophys. Res.*, *102*, 853–874.
Korenaga, J., and P. B. Kelemen (1997), Origin of gabbro sills in the Moho transition zone of the Oman ophiolite: Implications for magma transport in the oceanic lower crust, *J. Geophys. Res.*, *102*, 27,729–27,749, doi:10.1029/97JB02604.
Langmuir, C., J. Bender, and R. Batiza (1986), Petrological and tectonic segmentation of the East Pacific Rise, 5 30′–14 30′ N, *Nature*, *322*(6078), 422–429.
Langmuir, C., S. Humphris, and D. Fornari (1997), Hydrothermal vents near a mantle hot spot: The Lucky Strike vent field at 37°N on the Mid-Atlantic Ridge, *Earth Planet. Sci. Lett.*, *148*, 69–91.
Laubier, M., P. Schiano, R. Doucelance, L. Ottolini, and D. Laporte (2007), Olivine-hosted melt inclusions and melting processes beneath the FAMOUS zone (Mid-Atlantic Ridge), *Chem. Geol.*, *240*(1-2), 129–150.
Laubier, M., A. Gale, and C. H. Langmuir (2012), Melting and crustal processes at the FAMOUS segment (Mid-Atlantic Ridge): New insights from olivine-hosted melt inclusions from multiple samples, *J. Petrol.*, *53*(4), 665–698, doi:10.1093/petrology/egr075.
Le Roux, P., S. Shirey, E. Hauri, M. Perfit, and J. Bender (2006), The effects of variable sources, processes and contaminants on the composition of northern EPR MORB (8–10° N and 12–14° N): Evidence from volatiles (H_2O, CO_2, S) and halogens (F, Cl), *Earth Planet. Sci. Lett.*, *251*(3-4), 209–231.
Lee, C. T., P. Luffin, T. Plank, H. Dalton, and W. P. Leeman, (2009), Constraints on the depths and temperatures of basaltic magma generation on Earth and other terrestrial planets using new thermobarometers for mafic magmas, *Earth Planet. Sci. Lett.*, *279*, 20–33.
Lissenberg, C., and H. Dick (2008), Melt-rock reaction in the lower oceanic crust and its implications for the genesis of mid-ocean ridge basalt, *Earth Planet. Sci. Lett.*, *271*(1-4), 311–325.
Longhi, J. (2002), Some phase equilibrium systematics of lherzolite melting: I, *Geochem. Geophys. Geosyst.*, *3*(3), 1–33, doi:10.1029/2001GC000204.
McDonough, W., and S. Sun (1995), The composition of the earth, *Chem. Geol.*, *120*(3-4), 223–253.
Moreira, M., J. Escartín, E. Gayer, C. Hamelin, A. Bezos, F. Guillon, and M. Cannat (2011), Rare gas systematics on Lucky Strike basalts (37°N, North Atlantic): Evidence for efficient homogenization in a long-lived magma chamber system? *Geophys. Res. Lett.*, *38*, L08304, doi:10.1029/2011GL046794.
Morgan, J., and Y. J. Chen (1993), Dependence of ridge-axis morphology on magma supply and spreading rate, *Nature*, *364*(6439), 706–708.
Navin, D. A., C. Peirce, and M. C. Sinha (1998), The RAMESSES experiment-II. Evidence for accumulated melt beneath a slow spreading ridge from wide-angle refraction and multichannel reflection seismic profiles, *Geophys. J. Int.*, *135*(3), 746–772, doi:10.1046/j.1365-246X.1998.00709.x.
Newman, S., and J. Lowenstern (2002), VC: A silicate melt-H_2O-CO_2 solution model written in Visual Basic for excel*, *Computers & Geosciences*, *28*(5), 597–604.
Nicolas, A., and I. Reuber (1988), A new magma chamber model based on structural studies in the Oman ophiolite, *Tectonophysics*, *151*, 87–105.
Ondréas, H., M. Cannat, Y. Fouquet, A. Normand, P. M. Sarradin, and J. Sarrazin (2009), Recent volcanic events and the distribution of hydrothermal venting at the Lucky Strike hydrothermal field, Mid-Atlantic Ridge, *Geochem. Geophys. Geosyst.*, *10*, Q02006, doi:10.1029/2008GC002171.[19644118].
O'Neill, H. S. C., and F. E. Jenner (2012), The global pattern of trace-element distributions in ocean floor basalts, *Nature*, *491*(7426), 698–704, doi:10.1038/nature11678.
Parson, L., E. Gràcia, D. Coller, and C. German (2000), Second-order segmentation; The relationship between volcanism and tectonism at the MAR, 38°N–35°40′N, *Earth Planet. Sci. Lett.*, *178*, 231–251.
Perfit, M., and W. Chadwick Jr. (1998), Magmatism at mid-ocean ridges: Constraints from volcanological and geochemical investigations, in *Faulting and Magmatism at Mid-Ocean Ridges*, vol. 106, edited by W. Roger Buck et al., pp. 59–116, AGU, Washington, D. C.
Perfit, M., D. Fornari, M. Smith, J. Bender, C. Langmuir, and R. Haymon (1994), Small-scale spatial and temporal variations in mid-ocean ridge crest magmatic processes, *Geology*, *22*(4), 375–379.
Quick, J., and R. Denlinger (1993), Ductile deformation and the origin of layered gabbro in ophiolites, *J. Geophys. Res.*, *98*(B8), 14,015–14,027, doi:10.1029/93JB00698.
Roedder, E. (1984), Fluid inclusions, edited by P. H. Ribbe, *Rev. Mineral.*, *12*, 1–644.
Rubin, K., and J. Sinton (2007), Inferences on mid-ocean ridge thermal and magmatic structure from MORB compositions, *Earth Planet. Sci. Lett.*, *260*(1-2), 257–276.
Rubin, K. H., J. M. Sinton, J. Maclennan, and E. Hellebrand (2009), Magmatic filtering of mantle compositions at mid-ocean-ridge volcanoes, *Nat. Geosci.*, *2*(5), 321–328, doi:10.1038/ngeo504.
Seher, T., W. Crawford, S. Singh, and M. Cannat (2010), Crustal velocity structure of the Lucky Strike segment of the Mid-Atlantic Ridge at 37 N from seismic refraction measurements, *J. Geophys. Res.*, *115*, B03103, doi:10.1029/2009JB006650.
Shaw, A. M., E. H. Hauri, T. P. Fischer, D. R. Hilton, and K. A. Kelley (2008), Hydrogen isotopes in Mariana arc melt inclusions: Implications for subduction dehydration and the deep-Earth water cycle, *Earth Planet. Sci. Lett.*, *275*, 138–145, doi:10.1016/j.epsl.2008.08.015.
Shaw, A. M., M. D. Behn, S. E. Humphris, R. A. Sohn, and P. M. Gregg (2010), Deep pooling of low degree melts and volatile fluxes at the 85°E segment of the Gakkel Ridge: Evidence from olivine-hosted melt inclusions and glasses, *Earth Planet. Sci. Lett.*, *289*(3-4), 311–322, doi:10.1016/j.epsl.2009.11.018.

Shimizu, N. (1998), The geochemistry of olivine-hosted melt inclusions in a FAMOUS basalt ALV519-4-1, *Phys. Earth Planet. Int.*, *107*(1-3), 183–201.

Singh, S., W. Crawford, H. Carton, and T. Seher (2006), Discovery of a magma chamber and faults beneath a Mid-Atlantic Ridge hydrothermal field, *Nature*, *442*, 1029–1032.

Sinton, J., and R. Detrick (1992), Mid-ocean ridge magma chambers, *J. Geophys. Res.*, *97*(B1), 197–216, doi:10.1029/91JB02508.

Sinton, J. M., S. M. Smaglik, J. J. Mahoney, and K. C. Macdonald (1991), Magmatic processes at superfast spreading mid-ocean ridges: Glass compositional variations along the East Pacific Rise 13–23 S, *J. Geophys. Res.*, *96*(B4), 6133–6155, doi:10.1029/90JB02454.

Sobolev, A., and N. Shimizu (1993), Ultra-depleted primary melt included in an olivine from the Mid-Atlantic Ridge, *Nature*, *363*, 151–154.

Soule, S. A., D. S. Nakata, D. J. Fornari, A. T. Fundis, M. R. Perfit, and M. D. Kurz (2012), CO2 variability in mid-ocean ridge basalts from syn-emplacement degassing: Constraints on eruption dynamics, *Earth Planet. Sci. Lett.*, *327–328*(C), 39–49, doi:10.1016/j.epsl.2012.01.034.

Standish, J. J., H. J. B. Dick, P. J. Michael, W. G. Melson, and T. O'Hearn (2008), MORB generation beneath the ultraslow spreading Southwest Indian Ridge (9–25°E): Major element chemistry and the importance of process versus source, *Geochem. Geophys. Geosyst.*, *9*, Q05004, doi:10.1029/2008GC001959.

Stracke, A., and B. Bourdon (2009), The importance of melt extraction for tracing mantle heterogeneity, *Geochim. Cosmochim. Acta*, *73*(1), 218–238.

Su, Y., and C. H. Langmuir (2003), Global MORB chemistry compilation at the segment scale, PhD thesis, Dep. of Earth and Environ. Sci., Columbia Univ., N. Y.

Thibaud, R., P. Gente, and M. Maia (1998), A systematic analysis of the Mid-Atlantic Ridge morphology and gravity between 15°N and 40°N: Constraints of the thermal structure, *J. Geophys. Res.*, *103*(B10), 24,223–24,243, doi:10.1029/97JB02934.

Wanless, V. D., and A. M. Shaw (2012), Lower crustal crystallization and melt evolution at mid-ocean ridges, *Nat. Geosci.*, *5*(9), 651–655, doi:10.1038/ngeo1552.

Wanless, V. D., M. D. Behn, A. M. Shaw, and T. Plank (2014), Variations in melting dynamics and mantle compositions along the Eastern Volcanic Zone of the Gakkel Ridge: Insights from olivine-hosted melt inclusions, *Contrib. Mineral. Petrol.*, *167*(5), 1005, doi:10.1007/s00410-014-1005-7.

Workman, R. K., and S. R. Hart (2005), Major and trace element composition of the depleted MORB mantle (DMM), *Earth Planet. Sci. Lett.*, *231*(1-2), 53–72, doi:10.1016/j.epsl.2004.12.005.

Yang, T., Y. Shen, S. Vanderlee, S. Solomon, and S. Hung (2006), Upper mantle structure beneath the Azores hotspot from finite-frequency seismic tomography, *Earth Planet. Sci. Lett.*, *250*(1-2), 11–26, doi:10.1016/j.epsl.2006.07.031.